CrossMark

J. Fluid Mech. (2015), *vol.* 770, *pp.* 319–349. © Cambridge University Press 2015
doi:10.1017/jfm.2015.134

Modal and non-modal stability analysis of electrohydrodynamic flow with and without cross-flow

Mengqi Zhang[1,†], Fulvio Martinelli[2], Jian Wu[1], Peter J. Schmid[3] and Maurizio Quadrio[2]

[1]Département Fluides, Thermique, Combustion, Institut PPrime, CNRS-Université de Poitiers-ENSMA, UPR 3346, 43 Route de l'Aérodrome, Poitiers CEDEX F86036, France

[2]Dipartimento di Scienze e Tecnologie Aerospaziali, Politecnico di Milano, via La Masa 34, 20156 Milano, Italy

[3]Department of Mathematics, Imperial College London, London SW7 2AZ, UK

(Received 20 September 2014; revised 10 January 2015; accepted 26 February 2015; first published online 1 April 2015)

We report the results of a complete modal and non-modal linear stability analysis of the electrohydrodynamic flow for the problem of electroconvection in the strong-injection region. Convective cells are formed by the Coulomb force in an insulating liquid residing between two plane electrodes subject to unipolar injection. Besides pure electroconvection, we also consider the case where a cross-flow is present, generated by a streamwise pressure gradient, in the form of a laminar Poiseuille flow. The effect of charge diffusion, often neglected in previous linear stability analyses, is included in the present study and a transient growth analysis, rarely considered in electrohydrodynamics, is carried out. In the case without cross-flow, a non-zero charge diffusion leads to a lower linear stability threshold and thus to a more unstable flow. The transient growth, though enhanced by increasing charge diffusion, remains small and hence cannot fully account for the discrepancy of the linear stability threshold between theoretical and experimental results. When a cross-flow is present, increasing the strength of the electric field in the high-Re Poiseuille flow yields a more unstable flow in both modal and non-modal stability analyses. Even though the energy analysis and the input–output analysis both indicate that the energy growth directly related to the electric field is small, the electric effect enhances the lift-up mechanism. The symmetry of channel flow with respect to the centreline is broken due to the additional electric field acting in the wall-normal direction. As a result, the centres of the streamwise rolls are shifted towards the injector electrode, and the optimal spanwise wavenumber achieving maximum transient energy growth increases with the strength of the electric field.

Key words: instability, MHD and electrohydrodynamics

† Email address for correspondence: mengqi.zhang@univ-poitiers.fr

https://doi.org/10.1017/jfm.2015.134 Published online by Cambridge University Press

1. Introduction

1.1. *General description of electrohydrodynamic flow*

Electrohydrodynamics (EHD) is concerned with the interaction between an electric field and a flow field. Such configurations have broad applications in a range of industrial and biological devices. EHD effects can be used to enhance the heat transfer efficiency (Jones 1978; Allen & Karayiannis 1995), to design microscale EHD pumps (Bart *et al.* 1990; Darabi *et al.* 2002), to fabricate diagnostic devices and drug delivery systems (Chakraborty *et al.* 2009) and DNA microarrays (Lee *et al.* 2006), and to design new strategies for active flow control (Bushnell & McGinley 1989). Physically, EHD flow is characterized by a strong nonlinear interaction between the velocity field, the electric field and space charges: the electric force results in flow motion, which in turn affects the charge transport. The intricate nature of this nonlinearity defies a fundamental understanding of EHD flow. Moreover, as we will see, there still remains a mismatch or discrepancy between experimental observations and theoretical analysis.

One classic problem in EHD, named electroconvection, deals with the convective motions induced by unipolar charge injection into a dielectric liquid (of very low conductivity) that fills the gap between two parallel rigid plane electrodes. The Coulomb force acting on the free charge carriers tends to destabilize the system. Electroconvection is often compared to Rayleigh–Bénard convection (RBC) because of their similar geometry and convection patterns. Moreover, RBC is known to be analogous to the Taylor–Couette (TC) flow in the gap between two concentric rotating cylinders, where thermal energy transport in RBC corresponds to the transport of angular momentum in TC flow (Bradshaw 1969; Grossmann & Lohse 2000). In the linear regime of RBC, the flow is destabilized by the buoyancy force caused by the continued heating of the lower wall (an analogous role is played by centrifugal force in TC flow). As the thermal gradient exceeds a critical value, chaotic motion sets in. In EHD flow, the destabilizing factor is the electric force, acting in the wall-normal direction. However, the analogy between the two flows ends as soon as nonlinearities arise, especially where diffusive effects are concerned: in RBC, molecular diffusion constitutes the principal dissipative mechanism, whereas in EHD flow, it is the ion drift velocity KE (with K being the ionic mobility) that diffuses perturbations in the fluid. It is well known that RBC is of a supercritical nature, i.e. transition from the hydrostatic state to the finite-amplitude state occurs continuously as the controlling parameter, i.e. the Rayleigh number, is increased. For EHD flow, on the other hand, the bifurcation is subcritical, characterized by (i) an abrupt jump in motion amplitude from zero to a finite value, as a critical parameter is crossed, and (ii) the existence of a hysteresis loop. It is interesting to mention an analogy between EHD flow and polymeric flow: polymeric flow shows a hysteresis loop as well, as the first bifurcation is considered. In fact, the counterpart of EHD flow, i.e. magnetohydrodynamic (MHD) flow, has been compared to polymeric flow in Ogilvie & Proctor (2003).

Most studies in the EHD literature address electroconvection in the hydrostatic condition, i.e. without cross-flow. In this work we also investigate the EHD stability properties in the presence of cross-flow. Our interest is twofold. First, the potential of this flow configuration resides in the possibility of using the electric field to create large-scale rollers for flow manipulation; turbulent drag reduction designed in the spirit of Schoppa & Hussain (1998) and investigated by Soldati & Banerjee (1998) in the nonlinear regime is an example of this type. Secondly, EHD with cross-flow

https://doi.org/10.1017/jfm.2015.134 Published online by Cambridge University Press

has been applied to wire–plate electrostatic precipitators, but, owing to the complex nature of the chaotic interaction between wall turbulence and the electric field, our current understanding of such flows is rather limited. Nonlinear EHD simulations with a cross-flow component have been reported in Soldati & Banerjee (1998). More relevant to our linear problem is the unipolar-injection-induced instabilities in plane-parallel flows studied by Atten & Honda (1982) and Castellanos & Agrait (1992). The former work focused on so-called electroviscous effects, defined by an increase of viscosity due to the applied electric field compared to the canonical channel flow. The latter work found that, at high Reynolds numbers, the destabilizing mechanism is linked to inertia, while, at sufficiently low Reynolds numbers, EHD instabilities are dominant. In this article, we will not only address the modal stability problem of EHD channel flow, as those two previous studies did, but also take into account transient effects, discussed briefly below, of the high-Re channel flow in the presence of an electric field. Our results should be interesting to those researching flow instability and transition to turbulence, especially for high-Re flow. The results will also shed light on the study of flow control strategies using EHD effects.

1.2. *Stability of electrohydrodynamic flow*

The endeavour to understand stability and transition to turbulence in EHD flow dates back to the 1970s, when Schneider & Watson (1970) and Atten & Moreau (1972), among the first, performed a linear stability analysis on the flow of dielectric liquids confined between two parallel electrodes with unipolar injection of charges. The mechanism for linear instability could be explained via the formation of an electric torque engendered by the convective motion when the driving electric force is sufficiently strong to overcome viscous diffusion. It was established in Atten & Moreau (1972) that, in the weak-injection limit, $C \ll 1$, where C is the charge injection level, the flow is characterized by the criterion $T_c C^2 \approx 220.7$, where T_c is the linear stability criterion for the stability parameter T, defined in the mathematical modelling section (§ 2.2). In the case of space-charge-limited (SCL) injection, $C \to \infty$, they found $T_c \approx 160.75$. However, according to Lacroix, Atten & Hopfinger (1975) and Atten & Lacroix (1979), the experimentally determined stability criterion was notably different from the theoretical calculations. In the experiments performed by Atten & Lacroix (1979), the linear criterion was found to be $T_c \approx 100$ in the case of SCL, which is far lower than the theoretically predicted value. It was argued then that this disagreement might be due to neglect of charge diffusion (Atten 1976). We will address this discrepancy in the SCL case in this paper, and confirm that charge diffusion is indeed an important factor influencing the linear stability criterion in this case.

The first nonlinear stability analysis was performed by Félici (1971), who assumed a two-dimensional, *a priori* hydraulic model for the velocity field in the case of weak injection between two parallel plates. It was found that within the interval $[T_{nl}, T_c]$, where T_{nl} is the nonlinear stability criterion for T, two solutions exist, namely, a stable state and an unstable finite-amplitude state. This finding corroborated the fact that the bifurcation in the unipolar injection problem is of a subcritical nature and that the flow has a hysteresis loop, as experimentally verified by Atten & Lacroix (1979). Physically, this subcritical bifurcation is related to the formation of a region of zero charge (Pérez & Castellanos 1989). Later, this simple hydraulic model was

https://doi.org/10.1017/jfm.2015.134 Published online by Cambridge University Press

extended to three-dimensional hexagonal convective cells for the SCL case by Atten & Lacroix (1979), and it was shown that the most unstable hydrodynamic mode consists of hexagonal cells with the interior liquids flowing towards the injector. The nonlinear stability criterion for three-dimensional hexagonal cells, according to Atten & Lacroix (1979), was $T_{nl} \approx 90$ in the experiments, but theoretical studies produced $T_{nl} \approx 110$.

Most of the previous linear stability analyses of EHD flow focus on the most unstable mode of the linear system, which is insufficient for a comprehensive flow analysis. In fact, theoretically, the linear stability analysis is linked to the characteristics of the linearized Navier–Stokes (NS) operator $\boldsymbol{\mathcal{L}}$, which, in the case of shear flows (in this paper, the cross-flow case), may be highly non-normal, i.e. $\boldsymbol{\mathcal{L}}^{+}\boldsymbol{\mathcal{L}} \neq \boldsymbol{\mathcal{L}}\boldsymbol{\mathcal{L}}^{+}$ (with $\boldsymbol{\mathcal{L}}^{+}$ denoting the adjoint of $\boldsymbol{\mathcal{L}}$) or, expressed differently, the eigenvectors of the linear operator are mutually non-orthogonal (see Trefethen *et al.* 1993; Schmid & Henningson 2001). For a normal operator ($\boldsymbol{\mathcal{L}}^{+}\boldsymbol{\mathcal{L}} = \boldsymbol{\mathcal{L}}\boldsymbol{\mathcal{L}}^{+}$), the dynamics of the perturbations is governed by the most unstable mode over the entire time horizon. In contrast, a non-normal operator has the potential for large transient amplification of the disturbance energy in the early linear phase, even though the most unstable mode is stable. The theory of non-modal stability analysis (Farrell & Ioannou 1996; Schmid 2007), the main tool to be used in this work, has been applied successfully to explain processes active during transition to turbulence in several shear flows. The fact that the bifurcation of EHD flow is subcritical, a trait often observed in shear flows governed by non-normal linearized operators, tempts one to think that the discrepancy between the experimental value $T_c \approx 100$ and the theoretical value $T_c \approx 161$ in the SCL regime of EHD flow might be examined in the light of non-modal stability theory. In fact, it seems surprising that this type of stability analysis has so far only rarely been applied to EHD flows, except for the work of Atten (1974) in the case of hydrostatic flow. The method we employ here is different from Atten's quasi-stationary approach: non-modal stability theory, based on solving the initial-value problem, seeks the maximum disturbance energy growth over the entire time horizon when considering all admissible initial conditions and identifies the optimal initial condition for achieving this maximum energy growth. In Atten (1974), a quasi-stationary approach was taken that proposed that disturbances grow rapidly, compared to the time variation of the thickness of the unipolar layer; however, transient energy growth due to the non-normality of the linearized operator in hydrostatic EHD has been found to be rather limited in this work. This is in contrast with EHD Poiseuille flow, where non-normality is prevalent and should be considered from the outset.

The present paper extends the work by Martinelli, Quadrio & Schmid (2011) and is organized as follows. In § 2, we present the mathematical model, the governing equations and the framework of the linear stability analysis. In § 3, numerical details are given; and a code validation is provided in the appendix. We then present in § 4 the results of the modal and non-modal stability analysis, and in § 5 the energy analysis. Finally, in § 6, we summarize our findings and conclude with a discussion.

2. Problem formulation

2.1. *Mathematical modelling*

We consider the planar geometry sketched in figure 1, where the Cartesian coordinate system used in this work is (x, y, z) or $(\mathbf{1}_x, \mathbf{1}_y, \mathbf{1}_z)$ as the streamwise, wall-normal and spanwise directions, respectively. The two flat electrodes extend infinitely in the x and z directions, and the applied voltage only varies in the y direction. The distance

https://doi.org/10.1017/jfm.2015.134 Published online by Cambridge University Press

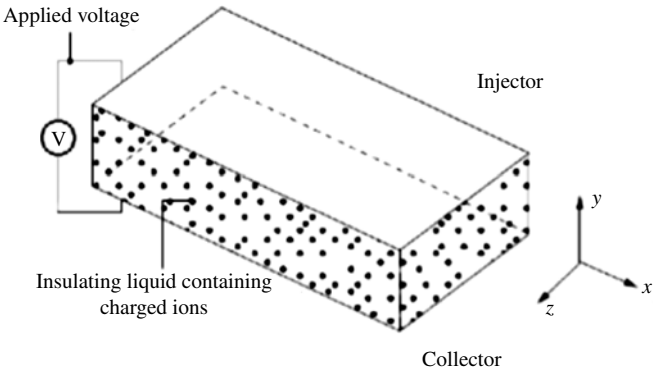


FIGURE 1. Sketch of the electroconvection problem with coordinate system (x, y, z). In the non-hydrostatic case, a flow rate is induced along the streamwise (x) direction.

between the two electrodes is $2L^*$. The dimensional variables and parameters are denoted with a superscript *. The electric field satisfies the reduced Maxwell equations. The charges are generated through electrochemical reactions on the charge-injecting electrode (Alj *et al.* 1985). Since the electric conductivity is very low, conduction currents are negligible even in the presence of large electric fields. Therefore, magnetic effects in the Maxwell equations can be neglected (Melcher 1981; Castellanos 1998), leading to the quasi-electrostatic limit of the Maxwell equations

$$\boldsymbol{\nabla}^* \times \boldsymbol{E}^* = 0, \tag{2.1a}$$

$$\boldsymbol{\nabla}^* \cdot \boldsymbol{D}^* = Q^*, \tag{2.1b}$$

$$\frac{\partial Q^*}{\partial t^*} + \boldsymbol{\nabla}^* \cdot \boldsymbol{J}^* = 0, \tag{2.1c}$$

where $\boldsymbol{E}^*$ is the electric field, $\boldsymbol{D}^* = \epsilon^* \boldsymbol{E}^*$ denotes the electric displacement, ϵ^* stands for the fluid permittivity, which we assume constant here, Q^* represents the charge density and $\boldsymbol{J}^*$ is the current density. Considering (2.1*a*), it is a well-known practice to define a potential field ϕ^* according to $\boldsymbol{E}^* = -\boldsymbol{\nabla}^* \phi^*$. Combining the first two equations, (2.1*a*) and (2.1*b*), we can write the governing equation for ϕ^* as

$$\nabla^{*2} \phi^* = -\frac{Q^*}{\epsilon^*}. \tag{2.2}$$

The current density $\boldsymbol{J}^*$ arises from several sources. By modelling the EHD flow with only one ionic species in a perfectly insulating fluid (conductivity $\sigma^* = 0$), one can express $\boldsymbol{J}^*$ as (Castellanos 1998)

$$\boldsymbol{J}^* = K^* \boldsymbol{E}^* Q^* + \boldsymbol{U}^* Q^* - D_v^* \boldsymbol{\nabla}^* Q^*, \tag{2.3}$$

where the first term accounts for the drift of ions (with respect to the fluid) under the effect of the electric field, moving at the relative velocity $K^* \boldsymbol{E}^*$, with K^* as the ionic mobility, the second term represents the convection of ions due to the fluid velocity $\boldsymbol{U}^*$, and the last term takes into account the charge diffusion, with D_v^* as the diffusion coefficient. Since the work of Pérez & Castellanos (1989), the vast body of literature, with the exception of Kourmatzis & Shrimpton (2012) for turbulent EHD

https://doi.org/10.1017/jfm.2015.134 Published online by Cambridge University Press

flow, neglects the charge diffusion term because of its small value when compared to the drift terms. However, we will show that, even though the numerical value of D_v^* is very small, its impact on the flow dynamics is undeniable.

The flow field is incompressible, viscous and Newtonian and governed by the NS equations, which, in vector notation, read

$$\boldsymbol{\nabla}^* \cdot \boldsymbol{U}^* = 0, \tag{2.4a}$$

$$\rho^* \frac{\partial \boldsymbol{U}^*}{\partial t^*} + \rho^* (\boldsymbol{U}^* \cdot \boldsymbol{\nabla}^*) \boldsymbol{U}^* = -\boldsymbol{\nabla}^* P^* + \mu^* \nabla^{*2} \boldsymbol{U}^* + \boldsymbol{F}_q^*, \tag{2.4b}$$

where $\boldsymbol{U}^*$ is the velocity field, P^* the pressure, ρ^* the density, $\mu^* = \rho^* \nu^*$ the dynamic viscosity (ν^* the kinematic viscosity) and $\boldsymbol{F}_q^*$ the volumetric density of electric force, which expresses the coupling between the fluid and the electric field. In general, $\boldsymbol{F}_q^*$ can be written as

$$\boldsymbol{F}_q^* = Q^* \boldsymbol{E}^* - \frac{1}{2} |\boldsymbol{E}^*|^2 \boldsymbol{\nabla}^* \epsilon^* + \boldsymbol{\nabla}^* \left[\frac{|\boldsymbol{E}^*|^2}{2} \rho^* \frac{\partial \epsilon^*}{\partial \rho^*} \right], \tag{2.5}$$

where the three terms on the right-hand side represent, respectively, the Coulomb force, the dielectric force and the electrostrictive force. The Coulomb force is commonly the strongest force when a DC voltage is applied. As we assume an isothermal and homogeneous fluid, the permittivity ϵ is constant in space. As a result, the dielectric force is zero (however, it would be dominant in the case of an AC voltage). The electrostrictive force can be incorporated into the pressure term of the NS equation, as it can be expressed as the gradient of a scalar field. Therefore, the only remaining term of interest in our formulation is the Coulomb force.

The system is supplemented by suitable boundary conditions. In our problem, we assume periodic boundary conditions in the wall-parallel directions. The no-slip and no-penetration conditions for the velocities are assumed at the channel walls. For the potential field, we require Dirichlet conditions on both walls, on the injector $\phi^*(L^*) = \phi_0^*$ and the collector $\phi^*(-L^*) = 0$ in order to fix the potential drop $\Delta\phi_0^*$ between the electrodes. The injection mechanism is autonomous and homogeneous, meaning that the charge density is constant on the injector, not influenced by the nearby electric field and has a zero wall-normal flux of charge on the collector, i.e. $Q^*(L^*) = -Q_0^*$ and $(\partial Q^*/\partial y^*)(-L^*) = 0$. Owing to the homogeneity in the wall-parallel directions, there is no requirement for boundary conditions in the x and z directions.

2.2. *Non-dimensionalized governing equations*

In the no-cross-flow case, as we are interested in the effect of the electric field on the flow dynamics, we non-dimensionalize the full system with the characteristics of the electric field, i.e. L^* (half-distance between the electrodes), $\Delta\phi_0^*$ (voltage difference applied to the electrodes) and Q_0^* (injected charge density). Accordingly, the time t^* is non-dimensionalized by $L^{*2}/(K^* \Delta\phi_0^*)$, the velocity $\boldsymbol{U}^*$ by $K^* \Delta\phi_0^*/L^*$, the pressure P^* by $\rho_0^* K^{*2} \Delta\phi_0^{*2}/L^{*2}$, the electric field $\boldsymbol{E}^*$ by $\Delta\phi_0^*/L^*$ and the electric density Q^* by Q_0^*. Therefore, the non-dimensional equations read

$$\boldsymbol{\nabla} \cdot \boldsymbol{U} = 0, \tag{2.6a}$$

$$\frac{\partial \boldsymbol{U}}{\partial t} + (\boldsymbol{U} \cdot \boldsymbol{\nabla}) \boldsymbol{U} = -\boldsymbol{\nabla} P + \frac{M^2}{T} \nabla^2 \boldsymbol{U} + C M^2 Q \boldsymbol{E}, \tag{2.6b}$$

https://doi.org/10.1017/jfm.2015.134 Published online by Cambridge University Press

$$\frac{\partial Q}{\partial t} + \nabla \cdot [(\boldsymbol{E} + \boldsymbol{U})Q] = \frac{1}{Fe}\nabla^2 Q, \tag{2.6c}$$

$$\nabla^2 \phi = -CQ, \tag{2.6d}$$

$$\boldsymbol{E} = -\nabla \phi, \tag{2.6e}$$

where

$$M = \frac{(\epsilon^*/\rho_0^*)^{1/2}}{K^*}, \quad T = \frac{\epsilon^* \Delta\phi_0^*}{K^* \mu^*}, \quad C = \frac{Q_0^* L^{*2}}{\Delta\phi_0^* \epsilon^*}, \quad Fe = \frac{K^* \Delta\phi_0^*}{D_v^*}. \tag{2.7a–d}$$

Additionally, the non-dimensional boundary conditions are $\boldsymbol{U}(\pm 1) = 0$, $\phi(1) = 1$, $\phi(-1) = 0$, $Q(1) = -1$ and $(\partial Q/\partial y)(-1) = 0$.

Various dimensionless groups appear in the equations as written above. First, M is the ratio between the hydrodynamic mobility $(\epsilon^*/\rho_0^*)^{1/2}$ and the true ion mobility K^*. Gases usually take on a value of M less than 0.1 and liquids have values of M greater than 1 (Castellanos & Agrait 1992). Second, Taylor's parameter T represents the ratio of the Coulomb force to the viscous force. It is the principal stability parameter, assuming a similar role as the Rayleigh number in RBC. Next, C measures the injection level. When $C \gg 1$, the system is in a strong-injection regime, and when $C \ll 1$, it is in a weak-injection regime. Finally, Fe is the reciprocal of the charge diffusivity coefficient. The factor M^2/T appearing in (2.6*b*) can be interpreted as the ratio between the charge relaxation time $L^{*2}/(K^* \Delta\phi_0^*)$ by drift and the momentum relaxation time L^{*2}/ν^*. This mathematical model for EHD flow has been assumed and studied in many previous investigations of linear stability and turbulence analyses for a dielectric liquid subject to unipolar injection of ions (Lacroix *et al.* 1975; Traoré & Pérez 2012; Wu *et al.* 2013), except that the diffusion term in (2.6*c*) is usually neglected (excluding the study of Kourmatzis & Shrimpton 2012).

2.3. *Linear stability problem*

The linear problem is obtained by decomposing the flow variable as a sum of base state and perturbation, i.e. $\boldsymbol{U} = \bar{\boldsymbol{U}} + \boldsymbol{u}$, $P = \bar{P} + p$, $\boldsymbol{E} = \bar{\boldsymbol{E}} + \boldsymbol{e}$, $\boldsymbol{D} = \bar{\boldsymbol{D}} + \boldsymbol{d}$, $Q = \bar{Q} + q$ and $\phi = \bar{\phi} + \varphi$. For the vector fields, we have $\boldsymbol{u} = (u, v, w)$ and $\boldsymbol{e} = (e_1, e_2, e_3)$ along the three Cartesian coordinate directions. After substituting the decompositions into the governing equations (2.6*a–e*), subtracting from them the governing equations for the base states and retaining the terms of first order, the linear system reads

$$\nabla \cdot \boldsymbol{u} = 0, \tag{2.8a}$$

$$\frac{\partial \boldsymbol{u}}{\partial t} + (\boldsymbol{u} \cdot \nabla)\bar{\boldsymbol{U}} + (\bar{\boldsymbol{U}} \cdot \nabla)\boldsymbol{u} = -\nabla p + \frac{M^2}{T}\nabla^2 \boldsymbol{u} + CM^2(q\bar{\boldsymbol{E}} + \bar{Q}\boldsymbol{e}), \tag{2.8b}$$

$$\frac{\partial q}{\partial t} + \nabla \cdot [(\bar{\boldsymbol{E}} + \bar{\boldsymbol{U}})q + (\boldsymbol{e} + \boldsymbol{u})\bar{Q}] = \frac{1}{Fe}\nabla^2 q, \tag{2.8c}$$

$$\nabla^2 \varphi = -Cq, \tag{2.8d}$$

$$\boldsymbol{e} = -\nabla \varphi, \tag{2.8e}$$

with the boundary conditions for the fluctuations $\boldsymbol{u}(\pm 1) = 0$, $\varphi(\pm 1) = 0$, $q(1) = 0$ and $(\partial q/\partial y)(-1) = 0$.

https://doi.org/10.1017/jfm.2015.134 Published online by Cambridge University Press

2.3.1. *Base states*

The base states are the solutions to (2.6*a–e*) in the case of no time dependence. Owing to the periodicity in the wall-parallel directions, we can reduce the shape of the base states as functions of y only, that is, $\bar{\boldsymbol{U}} = \bar{U}(y)\mathbf{1}_y$ and $\bar{\boldsymbol{E}} = \bar{E}(y)\mathbf{1}_y$. For the base flow $\bar{U}(y)$, we are interested in the hydrostatic and pressure-driven Poiseuille flows, which, after non-dimensionalization, are given by

$$\bar{U}(y) = 0, \quad \bar{U}(y) = Re\frac{M^2}{T}(1-y^2) = (1-y^2), \tag{2.9a,b}$$

respectively, in which the (electric) Reynolds number is defined as $Re = T/M^2 = K^*\Delta\phi_0^*/\nu^*$ (in order to enforce the same constant flow rate). It is a passive parameter in the hydrostatic case, but becomes a free parameter in the presence of high-Re cross-flow, in which, consequently, M would be the passive parameter. Therefore, in the Poiseuille flow case, we modify the governing equation (2.8*b*) by substituting the relation $Re = T/M^2$ to obtain

$$\frac{\partial \boldsymbol{u}}{\partial t} + (\boldsymbol{u}\cdot\boldsymbol{\nabla})\bar{\boldsymbol{U}} + (\bar{\boldsymbol{U}}\cdot\boldsymbol{\nabla})\boldsymbol{u} = -\boldsymbol{\nabla}p + \frac{1}{Re}\nabla^2\boldsymbol{u} + \frac{CT}{Re}(q\bar{\boldsymbol{E}} + \bar{Q}\boldsymbol{e}). \tag{2.10}$$

By doing so, it is more obvious to identify the effects of T and C on the electric force term. The parameter $Re = K^*\Delta\phi_0^*/\nu^*$ here coincides with the canonical hydrodynamic equivalent $Re_h = U^*L^*/\nu^*$ because of the electric scaling we chose. However, in a general sense, the two may not necessarily be identical. The non-dimensional quantity

$$\frac{Re}{Re_h} = \frac{K^*\Delta\phi_0^*}{U^*L^*} = \frac{L^*/U^*}{L^{*2}/(K^*\Delta\phi_0^*)} \tag{2.11}$$

relates the eddy turnover time and the charge relaxation time by the drift. According to the equality $T = Re\,M^2$, when Re is near linear criticality at 5772 and T is around 10^2, $M \approx 0.1$. This implies that the working liquid is gas. Moreover, in contrast to the nonlinear constitutive modelling for polymers in viscoelastic flow, the base flow is not modified under the influence of the base electric field, even though the coupling between $\boldsymbol{U}$ and Q is nonlinear in (2.6*c*). This is because the directions of the base flow and the base electric field are perpendicular. Nevertheless, the base pressure gradient in the wall-normal direction is no longer zero.

The base electric field $\bar{\boldsymbol{E}}(y)$ can be solved from (2.6*c–e*), recast into an equation for $\bar{\phi}$ only, which reads

$$\bar{\phi}'\bar{\phi}''' + (\bar{\phi}'')^2 + \frac{1}{Fe}\bar{\phi}'''' = 0, \tag{2.12}$$

where prime $'$ denotes the spatial derivative with respect to the y direction. The boundary conditions are $\bar{\phi}(1) = 1$, $\bar{\phi}(-1) = 0$, $\bar{\phi}''(1) = -C$ and $\bar{\phi}'''(-1) = 0$. Analytical solutions to this fourth-order ordinary differential equation can be obtained by observing that the equation can be transformed into a Riccati equation; alternatively, as we do here, a simple numerical integration combined with a nonlinear gradient method provides us with the required $\bar{\phi}(y)$ profile. The Poiseuille base flow and the base states of the electric and charge fields are shown in figure 2.

https://doi.org/10.1017/jfm.2015.134 Published online by Cambridge University Press

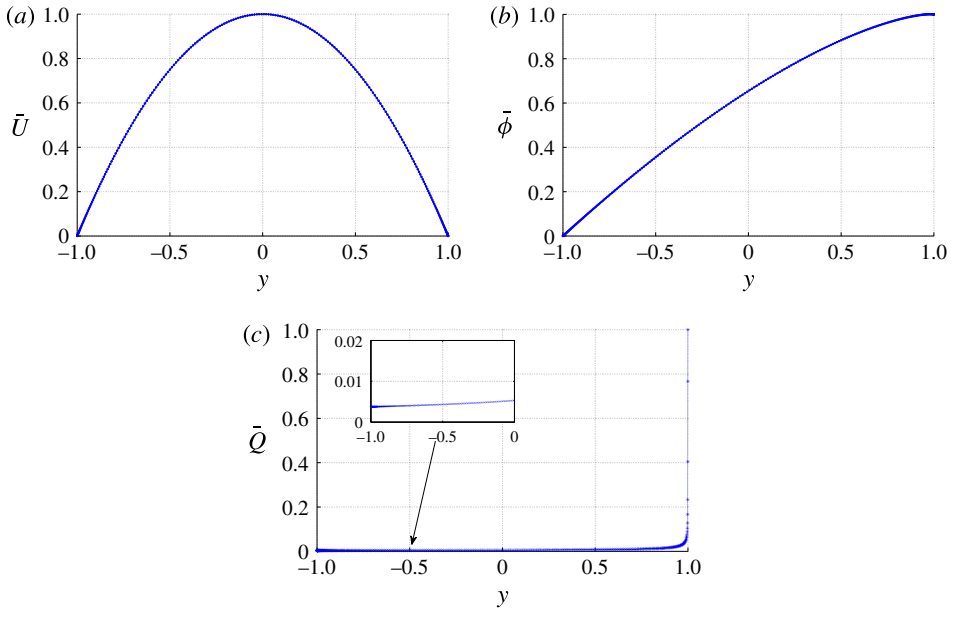


FIGURE 2. (Colour online) The base states: (*a*) $\bar{U}$, (*b*) $\bar{\phi}$ and (*c*) $\bar{Q}$.

2.3.2. *Matrix representation*

In linear stability analysis, it is a common practice to rewrite the fluid system (2.8*a*,*b*) in terms of the wall-normal velocity v and the wall-normal vorticity $\eta = \partial_z u - \partial_x w$ by eliminating the pressure term. For the electric field, the three equations (2.8*c*–*e*) can be reduced to one for φ. Therefore, the governing equations (2.8*a*–*e*) become, in terms of a v–η–φ formulation,

$$\frac{\partial \nabla^2 v}{\partial t} = \left[-\bar{U}\frac{\partial}{\partial x}\nabla^2 + \bar{U}''\frac{\partial}{\partial x} + \frac{M^2}{T}\nabla^4\right] v + M^2\left[-\bar{\phi}'''\left(\nabla^2 - \frac{\partial^2}{\partial y^2}\right)\varphi + \bar{\phi}'\left(\nabla^2 - \frac{\partial^2}{\partial y^2}\right)\nabla^2\varphi\right], \tag{2.13a}$$

$$\frac{\partial \eta}{\partial t} = -\bar{U}\frac{\partial}{\partial x}\eta - \bar{U}'\frac{\partial v}{\partial z} + \frac{M^2}{T}\nabla^2\eta, \tag{2.13b}$$

$$\frac{\partial \nabla^2 \varphi}{\partial t} = \bar{\phi}'\frac{\partial \nabla^2\varphi}{\partial y} + \bar{\phi}'''\frac{\partial \varphi}{\partial y} + 2\bar{\phi}''\nabla^2\varphi - \bar{U}\frac{\partial \nabla^2\varphi}{\partial x} - \bar{\phi}''' v + \frac{1}{Fe}\nabla^4\varphi, \tag{2.13c}$$

with boundary conditions

$$\left.\begin{array}{ccc} v(\pm1) = 0, & v'(\pm1) = 0, & \\ & \eta(\pm1) = 0, & \\ \varphi(\pm1) = 0, & \varphi''(1) = 0, & \varphi'''(-1) = 0. \end{array}\right\} \tag{2.14}$$

For compactness, we write $\boldsymbol{\gamma} = (v, \eta, \varphi)^{\mathrm{T}}$, and the linearized system, recast in matrix notation, becomes

$$\begin{pmatrix} \nabla^2 & \boldsymbol{0} & \boldsymbol{0} \\ \boldsymbol{0} & \boldsymbol{I} & \boldsymbol{0} \\ \boldsymbol{0} & \boldsymbol{0} & \nabla^2 \end{pmatrix} \frac{\partial}{\partial t}\begin{pmatrix} v \\ \eta \\ \varphi \end{pmatrix} = \begin{pmatrix} \boldsymbol{L}_{os} & \boldsymbol{0} & \boldsymbol{L}_{v\varphi} \\ \boldsymbol{L}_{c} & \boldsymbol{L}_{sq} & \boldsymbol{0} \\ \boldsymbol{L}_{\varphi v} & \boldsymbol{0} & \boldsymbol{L}_{\varphi\varphi} \end{pmatrix}\begin{pmatrix} v \\ \eta \\ \varphi \end{pmatrix}, \tag{2.15}$$

https://doi.org/10.1017/jfm.2015.134 Published online by Cambridge University Press

where $\boldsymbol{I}$ denotes the identity matrix and the submatrices $\boldsymbol{L}_{os}$, $\boldsymbol{L}_{v\varphi}$, $\boldsymbol{L}_{c}$, $\boldsymbol{L}_{sq}$, $\boldsymbol{L}_{\varphi v}$ and $\boldsymbol{L}_{\varphi\varphi}$ can be easily deduced from (2.13*a–c*). To represent the system even more compactly, we can rewrite the linearized problem (2.15) as

$$\boldsymbol{\mathcal{A}}\frac{\partial \boldsymbol{\gamma}}{\partial t} = \boldsymbol{\mathcal{B}}\boldsymbol{\gamma} \quad \Longrightarrow \quad \frac{\partial \boldsymbol{\gamma}}{\partial t} = \boldsymbol{\mathcal{L}}\boldsymbol{\gamma}, \tag{2.16}$$

where $\boldsymbol{\mathcal{L}} = \boldsymbol{\mathcal{A}}^{-1}\boldsymbol{\mathcal{B}}$ represents the linearized NS operator for EHD flow.

Since the flow is homogeneous in the wall-parallel directions, the perturbations are assumed to take on a wave-like shape. Moreover, as we consider a linear problem with a steady base flow, it is legitimate to examine the frequency response of the linear system for each frequency individually. These two simplifications lead to

$$\boldsymbol{f}(x, y, z, t) = \hat{\boldsymbol{f}}(y, t)\exp(\mathrm{i}\alpha x + \mathrm{i}\beta z) = \tilde{\boldsymbol{f}}(y)\exp(-\mathrm{i}\omega t)\exp(\mathrm{i}\alpha x + \mathrm{i}\beta z), \tag{2.17}$$

where $\boldsymbol{f}$ could represent any flow variable in $(\boldsymbol{u}, p, \boldsymbol{e}, q, \varphi)^{\mathrm{T}}$, $\hat{\boldsymbol{f}}(y, t)$ and $\tilde{\boldsymbol{f}}(y)$ are the shape functions, α and β are the real-valued streamwise and spanwise wavenumbers, and the complex-valued ω is the circular frequency of the perturbation, with its real part ω_r representing the phase speed and its imaginary part ω_i representing the growth rate of the linear perturbation. Upon substitution of the above expression into the linear problem (2.16), we arrive at an eigenvalue problem for the v–η–φ formulation that reads

$$-\mathrm{i}\omega\tilde{\boldsymbol{\gamma}} = \boldsymbol{\mathcal{L}}\tilde{\boldsymbol{\gamma}}, \tag{2.18}$$

where $-\mathrm{i}\omega$ is the eigenvalue and $\tilde{\boldsymbol{\gamma}}$ is the corresponding eigenvector. Both formulations, (2.16) and (2.18), would be relevant as discussed in a recent review by Schmid & Brandt (2014). The least unstable eigenvalues obtained from the eigenproblem formulation (2.18) would determine the asymptotic behaviour of the linear system, while the initial-value problem formulation (2.16) could be used to examine the dynamics of the fluid system evolving over a finite time scale.

2.3.3. *Energy norm*

In our calculation of the non-modal transient growth, we define the total energy density of the perturbation contained in a control volume Ω as

$$\begin{aligned}\int_{\Omega}\mathcal{E}^{*}\mathrm{d}V^{*} &= \int_{\Omega}(\mathcal{E}_{k}^{*}+\mathcal{E}_{\varphi}^{*})\mathrm{d}V^{*} = \int_{\Omega}\frac{1}{2}(\rho_{0}^{*}\boldsymbol{u}^{*}\cdot\boldsymbol{u}^{*}+\boldsymbol{e}^{*}\cdot\boldsymbol{d}^{*})\mathrm{d}V^{*}\\ &= \int_{\Omega}\frac{1}{2}(\rho_{0}^{*}(u^{*2}+v^{*2}+w^{*2})+\epsilon^{*}|\nabla^{*}\varphi^{*}|^{2})\mathrm{d}V^{*}.\end{aligned} \tag{2.19}$$

The perturbed electric energy $\mathcal{E}_{\varphi}^{*}$ follows the definition in Castellanos (1998). In terms of the v–η–φ formulation, the non-dimensionalized energy norm in spectral space becomes

$$\begin{aligned}\int_{\Omega}\mathcal{E}\mathrm{d}V &= \frac{1}{2}\cdot\frac{1}{2}\int\hat{\boldsymbol{\gamma}}^{\dagger}\begin{pmatrix}\boldsymbol{I}+\dfrac{1}{k^{2}}\boldsymbol{D}_{1}^{\dagger}\boldsymbol{D}_{1} & \boldsymbol{0} & \boldsymbol{0}\\ \boldsymbol{0} & \dfrac{1}{k^{2}}\boldsymbol{I} & \boldsymbol{0}\\ \boldsymbol{0} & \boldsymbol{0} & M^{2}(k^{2}\boldsymbol{I}+\boldsymbol{D}_{1}^{\dagger}\boldsymbol{D}_{1})\end{pmatrix}\hat{\boldsymbol{\gamma}}\mathrm{d}y\\ &= \int_{\Omega}\hat{\boldsymbol{\gamma}}^{\dagger}\boldsymbol{M}\hat{\boldsymbol{\gamma}}\mathrm{d}y,\end{aligned} \tag{2.20}$$

https://doi.org/10.1017/jfm.2015.134 Published online by Cambridge University Press

where the superscript dagger † denotes the complex conjugate, $k^2 = \alpha^2 + \beta^2$, and $\boldsymbol{D}_1$ represents the first-derivative matrix with respect to the wall-normal direction (likewise for $\boldsymbol{D}_2$ and $\boldsymbol{D}_3$ below). The positive definite matrix $\boldsymbol{M}$ allows us to work in the L_2-norm. To do so, we apply a Cholesky decomposition to the weight matrix according to $\boldsymbol{M} = \boldsymbol{F}^\dagger \boldsymbol{F}$ and define $\hat{\boldsymbol{\xi}} = \boldsymbol{F}\hat{\boldsymbol{y}}$ to arrive at

$$\int_\Omega \mathcal{E}\,\mathrm{d}V = \int_\Omega \hat{\boldsymbol{y}}^\dagger \boldsymbol{M}\hat{\boldsymbol{y}}\,\mathrm{d}y = \int_\Omega \hat{\boldsymbol{y}}^\dagger \boldsymbol{F}^\dagger \boldsymbol{F}\hat{\boldsymbol{y}}\,\mathrm{d}y = \int_\Omega \hat{\boldsymbol{\xi}}^\dagger \hat{\boldsymbol{\xi}}\,\mathrm{d}y = \|\hat{\boldsymbol{\xi}}\|_2, \tag{2.21}$$

where $\|\cdot\|_2$ represents the L_2-norm and, accordingly, the eigenvalue problem (2.18) becomes

$$-\mathrm{i}\omega(\boldsymbol{F}\hat{\boldsymbol{y}}) = \boldsymbol{F}\boldsymbol{\mathcal{L}}\boldsymbol{F}^{-1}(\boldsymbol{F}\hat{\boldsymbol{y}}). \tag{2.22}$$

Therefore, once the linear operator is redefined as $\boldsymbol{\mathcal{L}}_{L_2} = \boldsymbol{F}\boldsymbol{\mathcal{L}}\boldsymbol{F}^{-1}$, we can conveniently use the L_2-norm and its associated inner product for all computations. The transient growth G, defined as the maximum energy growth over all possible initial conditions $\hat{\boldsymbol{\xi}}_0$, is given below in the L_2-norm,

$$G(t) = \max_{\hat{\boldsymbol{\xi}}_0} \frac{\|\hat{\boldsymbol{\xi}}(t)\|_2}{\|\hat{\boldsymbol{\xi}}(0)\|_2} = \max_{\hat{\boldsymbol{\xi}}_0} \frac{\|\boldsymbol{\mathcal{T}}\hat{\boldsymbol{\xi}}(0)\|_2}{\|\hat{\boldsymbol{\xi}}(0)\|_2} = \|\boldsymbol{\mathcal{T}}\|_2 = \|\mathrm{e}^{t\boldsymbol{F}\boldsymbol{\mathcal{L}}\boldsymbol{F}^{-1}}\|_2, \tag{2.23}$$

where $\boldsymbol{\mathcal{T}}$ is the linear evolution operator, i.e. the solution to (2.16).

The parameters that are to be investigated include the injection level C, the mobility parameter M, the charge diffusion coefficient Fe, the Taylor parameter T, the Reynolds number Re, and the streamwise and spanwise wavenumbers α and β.

3. Numerical method and validation

3.1. *Numerical method*

To discretize the eigenvalue problem (2.18), we use a spectral method based on collocation points chosen as the roots of Chebyshev polynomials. The MATLAB suite for partial differential equations by Weideman & Reddy (2000) is used for differentiation and integration.

To impose the boundary condition, we employ the boundary boarding technique (Boyd 2001), in which selected rows of the linear matrices are replaced directly by the boundary conditions. When solving the eigenvalue problem via the MATLAB routine `eig` with the above boundary condition enforced, we find that the eigenvalues converge for a sufficient number N of collocation points (see figure 12 and table 4 in the validation section in appendix A) and approach the pure hydrodynamic results as electric effects become negligible (see figure 13 and table 6). The corresponding eigenvectors, however, are incorrect, since they do not satisfy the proper boundary conditions (not shown). To overcome this difficulty, we employ an iterative technique to obtain the eigenvector associated with a specified eigenvalue. In the generalized eigenvalue problem (2.16), a desired eigenvalue ω (and its corresponding eigenvector) is targeted by applying the spectral transformation

$$\boldsymbol{\mathcal{S}} = (\boldsymbol{\mathcal{B}} - \omega\boldsymbol{\mathcal{A}}_1) \setminus \boldsymbol{\mathcal{A}}_1, \tag{3.1}$$

where $\boldsymbol{\mathcal{A}}_1 = -\mathrm{i}\boldsymbol{\mathcal{A}}$ and $\boldsymbol{\mathcal{S}}$ will be processed by an iterative routine (Saad 2011).

https://doi.org/10.1017/jfm.2015.134 Published online by Cambridge University Press

3.2. *Validation*

The stability problem for EHD flow is exceedingly challenging from a numerical point of view, which warrants a careful and thorough validation step, before results about stability characteristics, modal and non-modal solutions and physical mechanisms are produced. To conserve the clarity of the paper's structure, we postpone the validation steps to the appendix A.

4. Results of stability analysis

4.1. *Electrohydrodynamics without cross-flow*

As mentioned earlier, the parameter T plays the main role in determining the flow instability. The critical T_c denotes the minimum value of T within the linear regime, above which infinitesimal disturbances can grow exponentially in time; T_c will vary with the flow parameters. In the case of no cross-flow, the effects of Fe, T, M and C on the flow stability are investigated. As has already been assumed, the flow will be confined to the SCL regime, implying a large value for C.

We display the neutral stability curve in figure 3 for different Fe at $C = 50$, $M = 100$, $T = 155$, $\alpha = 2.5$ and $\beta = 0$. In the case without cross-flow, one does not need to distinguish between the x and z axes, since neither is preferred by the base flow $\bar{\boldsymbol{U}} = 0$; thus, we simply set $\beta = 0$. As mentioned in the validation section, results for $Fe = 10^7$ are very close to previous investigations. Even though the diffusion coefficient is small, it plays an important role in determining the critical T_c, as shown in figure 3(*a*,*b*). For example, for $Fe = 10^3$ the critical T_c declines to 140. In fact, the value of Fe could fall within the range 10^3–10^4 for real liquids (Pérez & Castellanos 1989), when Fe is non-dimensionalized in the same way as presented here. Physically, the effect of diffusion will smooth out sharp gradients in the flow. Unlike the unidirectional electric field pointing in the wall-normal direction, the diffusion effects act equally in all directions. With charge diffusion considered in the model, the discontinuous separatrix is blurred in the nonlinear phase (Pérez & Castellanos 1989). The physical mechanism of how charge diffusion influences the critical stability parameter T_c will be discussed by using an energy analysis (see § 5.1). In addition, the transient growth of disturbance energy has been discussed in Atten (1974) using the quasi-stationary method; transient energy growth has been confirmed as a minor factor in that work. This is also confirmed in our computations, as presented in figure 3(*c*): specifically, the figure shows that disturbance energy growth G reaches a value of approximately 3 at $T = 155$ for stable flows ($Fe > 10^3$).

The role of M in EHD is analogous to that of the Prandtl number in RBC. In figure 4(*a*), it is shown that the variation of M exerts no influence on the linear stability criterion, $T_c = 159.58$ at $C = 100$, $Fe = 10^5$, $\alpha = 2.57$ and $\beta = 0$; the same finding has been reported in Atten & Moreau (1972). For the transient dynamics, however, the same conclusion does not hold, as evidenced in figure 4(*b*). The plot describes a trend of increasing G_{max} with smaller M. The slopes at the final time are slightly different for each M, indicating that the asymptotic growth rates differ slightly (while the linear stability criterion remains the same).

Figure 5 depicts the influence on C, which measures the intensity of charge injection. Atten & Moreau (1972) and Atten & Lacroix (1979) reported a dependence of the critical value T_c on the parameter C. In figure 5(*a*), we see that, in the SCL regime, increasing C will yield lower T_c. This result can be understood from a

https://doi.org/10.1017/jfm.2015.134 Published online by Cambridge University Press

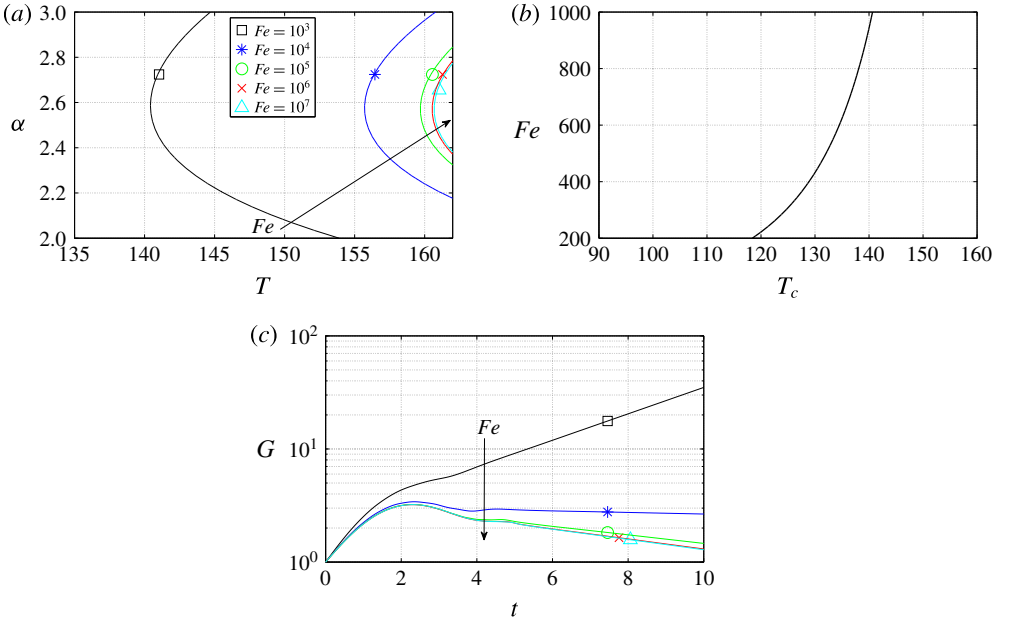


FIGURE 3. (Colour online) Effect of Fe: (a) neutral stability curves for various Fe: (b) T_c as a function of Fe; and (c) transient energy growth versus time. The parameters are $C = 50$, $M = 100$, $T = 155$, $\alpha = 2.5$, $\beta = 0$ and $N = 250$. The direction of the arrow indicates increasing Fe.

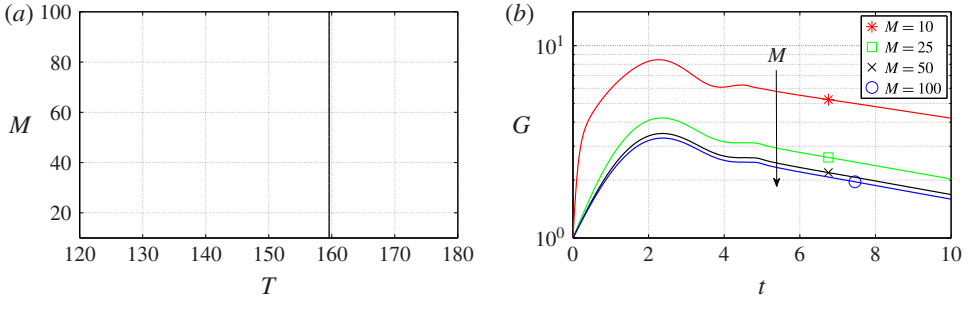


FIGURE 4. (Colour online) Effect of M: (a) neutral stability curve; and (b) transient energy growth versus time for different M and $T = 155$. The parameters are $C = 100$, $Fe = 10^5$, $\alpha = 2.57$, $\beta = 0$ and $N = 250$ without cross-flow. The direction of the arrow indicates increasing M.

physical argument. Increasing the intensity of charge injection will lead to a higher concentration of charges between the electrodes. The linear instability mechanism, as discussed above, relies on the formation of an electric torque due to convective motions. With higher charge concentration, the electric torque is stronger. Therefore, a lower voltage difference is required, which amounts to stating that a lower T will be sufficient to form an electric torque of comparable strength. But as we are in the SCL regime (with a value of $C = 50$ considered very large), a rise of C to 200 only yields a minor decrease in T_c. In contrast, the transient dynamics of the perturbation

https://doi.org/10.1017/jfm.2015.134 Published online by Cambridge University Press

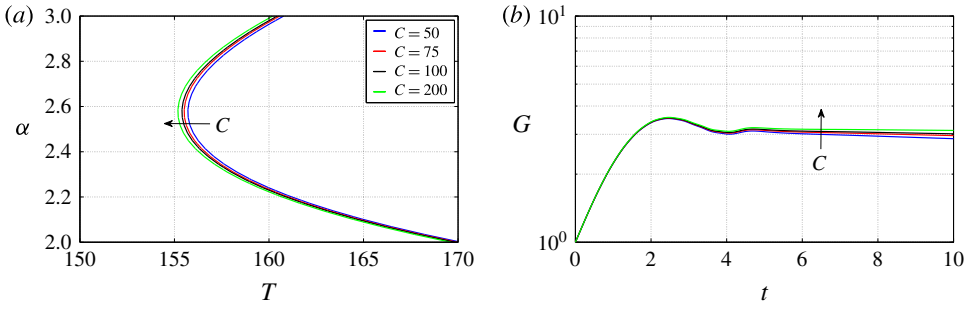


FIGURE 5. (Colour online) Effect of C: (a) neutral stability curve for four different injection levels C within the SCL regime; and (b) transient energy growth for different C at $T = 155$ and $\alpha = 2.57$. The parameters are $M = 100$, $Fe = 10^4$, $\beta = 0$ and $N = 250$, without cross-flow. The direction of the arrow indicates increasing C.

energy G appears not to be influenced by a change in C for early times; for example, see the time interval $t \in [0, 3]$ in figure 5(b).

4.2. *Electrohydrodynamics with cross-flow*

When cross-flow is considered, the property of the linearized system changes due to the presence of a base shear in the flow. Especially, this shear will render the linearized operator 'more non-normal'. We first note that, in the modal stability analysis, Squire's theorem still holds for EHD Poiseuille flow, that is, a two-dimensional instability will be encountered first. This can be easily verified by a perfect analogy with standard viscous theory (Schmid & Henningson 2001). Moreover, there are two sets of scales in the EHD problem with cross-flow. To study the influence of the cross-flow on the electric and the charge fields, the values of M and T are kept in the vicinity of the values in the previous section: the scale of the electric field will be considered primarily, whereas, when we examine the effects of the electric field exerted on the canonical Poiseuille flow, we take the value of the free parameter Re around 5772, i.e. the linear stability criterion for pressure-driven flow; the latter choice introduces a scale based on the hydrodynamics. In both cases, we will enforce the relation $Re = T/M^2$, which results in the Reynolds number Re being rather low in the former case (denoted as the low-Re case) and relatively high in the latter case (referred to as the high-Re case).

4.2.1. *Electrohydrodynamics: low Re*

We have demonstrated that non-modal effects in hydrostatic EHD are not significant. In the presence of cross-flow, given that the Reynolds number in this section is considered small, we expect the non-normality to be rather moderate as well. For this reason, we will mainly focus on the modal stability characteristics for the low-Re case.

In figure 6(a), it is observed that the symmetry of the hydrostatic EHD spectrum is now broken due to the presence of cross-flow. The most unstable perturbation travels at a positive phase speed $u_p = \omega_r/\alpha = 2.256/2.57 = 0.8778$, induced by cross-flow convection (the centreline velocity of the cross-flow is 1, as we set $Re = T/M^2$ in (2.9)). In figure 6(b), we show the neutral stability curve for $C = 50$, $M = 100$, $\beta = 0$ and $N = 250$, which can be directly compared to the results in figure 3. Note that,

https://doi.org/10.1017/jfm.2015.134 Published online by Cambridge University Press

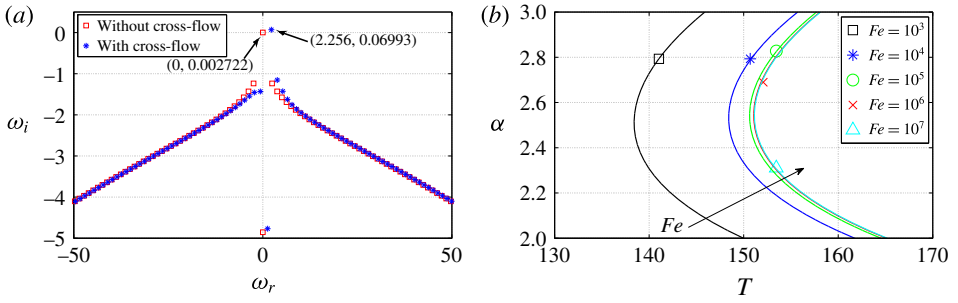


FIGURE 6. (Colour online) (*a*) Spectra for the case with and without cross-flow for $C = 50$, $M = 100$, $Fe = 10^5$, $T = 160$, $Re = T/M^2 = 0.016$ (for cross-flow), $\alpha = 2.57$, $\beta = 0$ and $N = 250$. (*b*) Effect of Fe on the neutral stability curve. The parameters are $C = 50$, $M = 100$, $\beta = 0$ and $N = 250$, with cross-flow. The direction of the arrow indicates increasing Fe.

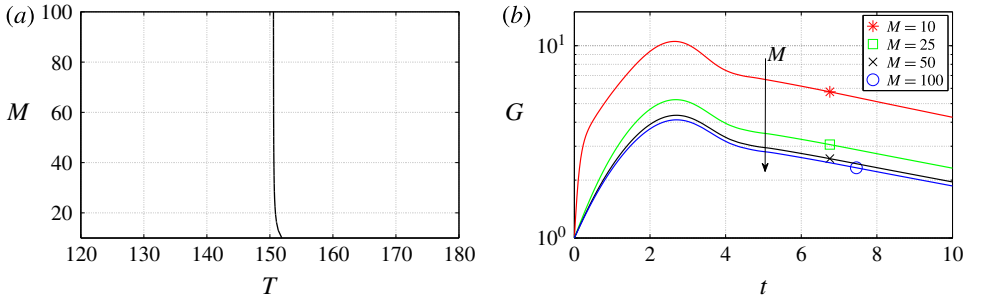


FIGURE 7. (Colour online) Effect of M: (*a*) neutral stability curve with cross-flow for $C = 100$, $Fe = 10^5$, $\alpha = 2.57$, $\beta = 0$ and $N = 250$; and (*b*) transient energy growth for different M and $T = 145$. The direction of the arrow indicates increasing M.

since $Re = T/M^2$ is enforced, the Reynolds number Re is not identical for each point, but generally small. We see that, with cross-flow, the critical T_c decreases compared to the no-cross-flow case; this indicates that the flow is more unstable in the presence of a low-Re cross-flow compared to the results in figure 3(*a*). To investigate the reason behind this destabilization, we again resort to an energy analysis in § 5.1.2. Previously, an energy analysis for EHD with cross-flow has been studied in Castellanos & Agrait (1992).

Even though varying M has no effect on the linear stability when $\bar{U} = 0$, as has been discussed briefly in the previous section, in the presence of cross-flow, changing M does influence the linear stability. This is displayed in figure 7(*a*), where we see that the effects of M are only discernible when M is small. We will discuss this issue further in the energy analysis section (§ 5.1.2). Considering non-normal linear stability, transient energy growth G is still small, even though slightly higher than in the no-cross-flow case.

4.2.2. *Electrohydrodynamics: high Re*

In this section, we consider the flow governed by the inertial scale, i.e. in the high-Re regime. To discuss the results more properly, the Reynolds number Re will be the

https://doi.org/10.1017/jfm.2015.134 Published online by Cambridge University Press

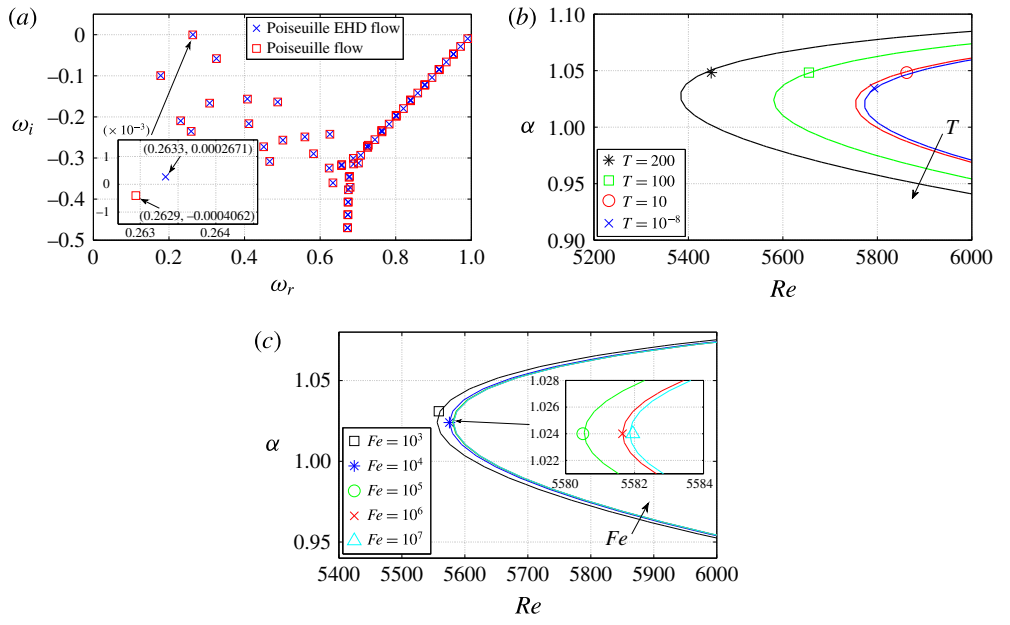


FIGURE 8. (Colour online) (*a*) Comparison of two spectra for $T = 10^{-8}$ and $T = 200$ at $C = 100$, $Re = 5600$, $Fe = 10^5$, $\alpha = 1$ and $\beta = 0$. (*b*) Effect of T on the neutral stability curve with cross-flow at $C = 100$, $Fe = 10^5$, $M = \sqrt{T/Re}$ and $\beta = 0$. The direction of the arrow indicates increasing T. (*c*) Effect of Fe on the neutral stability curve with cross-flow at $C = 100$, $T = 100$, $M = \sqrt{T/Re}$ and $\beta = 0$. The direction of the arrow indicates increasing Fe.

free parameter, and the governing momentum equation is given by (2.10); see § 2.3. The modal stability is examined in figure 8. In panel (*a*), changes in the spectrum due to the additional electric field are visible. It appears that the core modes, wall modes and centre modes do not change appreciably, except that the growth rate of the most unstable mode increases. In panel (*b*), we plot the neutral stability curve for varying T. The pure hydrodynamic linear stability limit $Re = 5772.2$ is recovered by considering a minute value for T such as $T = 10^{-8}$ (we could have taken $T = 0$, but to be compatible with (2.8) and the discussion based on that equation in other literature, we assign to T a negligibly small value). With increasing T, the system becomes more unstable, as the critical linear stability criterion becomes smaller. The reason for this is obviously due to the effect of the electric field transferring energy into the velocity fluctuations, while at the same time modifying the canonical channel flow; see table 3 in the energy analysis section (§ 5.1.3) at $C = 100$, $Fe = 10^5$, $Re = 5500$, $\alpha = 1$ and $\beta = 0$.

We also investigate the effect of charge diffusion Fe on the flow stability. The results concerning the neutral stability curve are shown in figure 8(*c*) at $C = 100$, $T = 100$, $M = \sqrt{T/Re}$ and $\beta = 0$. For small charge diffusion (large Fe), the critical Reynolds number Re is only slightly affected by changes in Fe. Only when $Fe = 10^3$ does the critical Reynolds number Re drop noticeably, though the destabilization effect is still small. It can thus be concluded that charge diffusion has only a small influence

https://doi.org/10.1017/jfm.2015.134 Published online by Cambridge University Press

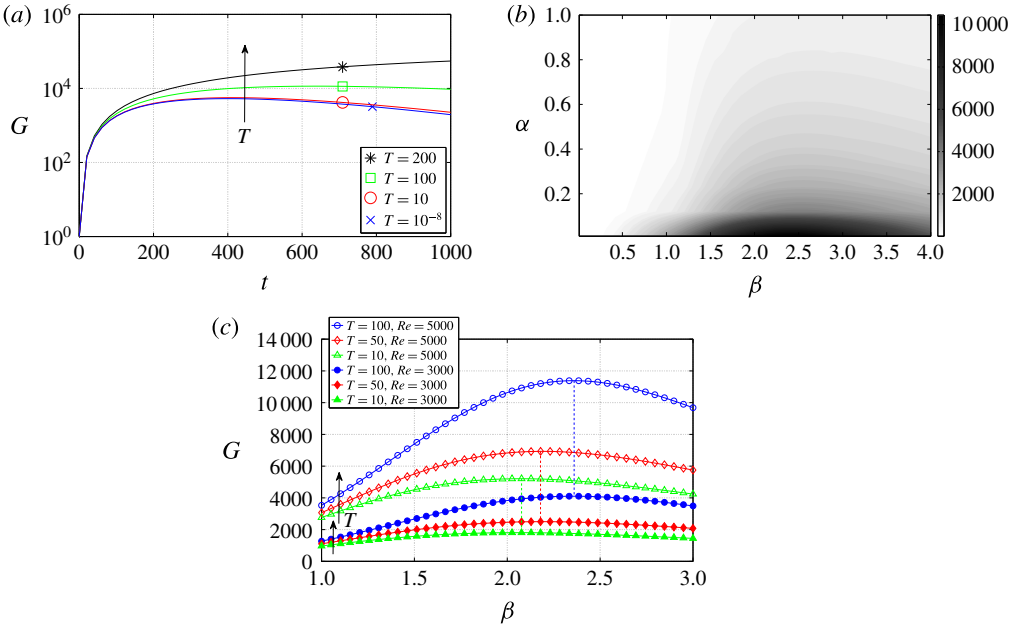


FIGURE 9. (Colour online) Effect of T: (a) transient energy growth for $C = 100$, $Re = 5200$, $Fe = 10^5$, $\alpha = 0$ and $\beta = 2$; (b) contours of transient growth G in the α–β plane at $C = 100$, $Re = 5000$, $Fe = 10^5$ and $T = 100$; and (c) transient growth G as a function of β at $C = 100$, $Fe = 10^5$ and $\alpha = 0$. The direction of the arrow indicates increasing T.

on the dynamics of EHD cross-flow at high Re. This is due to the inertial scale we are considering. As we have seen in the hydrostatic EHD flow, the effect of charge diffusion is significant, considering the electric scale, i.e. at relatively small (or zero) Reynolds numbers.

It is well known that in high-Re Poiseuille flow the two-dimensional Orr mechanism is not the principal mechanism for perturbation energy growth over a finite time horizon. The flow is expected to become turbulent within a short time interval, even though the asymptotic growth rate of the linear system is negative. The non-normal nature of the linearized NS operator for channel flow – in physical terms, due to the base flow modulation by spanwise vorticity tilting into the wall-normal direction – suggests that transient disturbance growth during the early phase should be considered primarily.

In figure 9(a), we present the transient growth G for different T. Mainly, the effect of increasing T is to enhance transient growth. The optimal initial condition that achieves maximum transient growth is shown in figure 9(b). The optimal wavenumbers for the pure hydrodynamic case, independent of Re, are found to be $\alpha = 0$ and $\beta = 2.05$, suggesting streamwise-independent vortices as the most amplified structures (Schmid & Henningson 2001). For high-Re EHD with cross-flow, the maximum transient growth is still found to favour streaks ($\alpha = 0$), but with a different optimal spanwise wavenumber of $\beta = 2.36$ at $C = 100$, $Re = 5000$, $Fe = 10^5$ and $T = 100$ (see figure 9b). Interestingly, for a different value of T, i.e. a different amount of

https://doi.org/10.1017/jfm.2015.134 Published online by Cambridge University Press

potential drop across the electrodes, the optimal wavenumber would be different. For example, at $T = 50$ the optimal $\beta = 2.18$, while at $T = 10$ the optimal $\beta = 2.08$, as shown in figure 9(*c*). It seems that, for smaller T, approaching the regime of pure hydrodynamics, the optimal β converges towards $\beta = 2.05$. The independence of maximum transient growth on Re for various β still holds in the limit of high-Re EHD flow, as indicated by the dashed lines connecting the peaks of the two curves for $Re = 5000$ and $Re = 3000$ in figure 9(*c*). In the nonlinear regime of EHD Poiseuille flow, the influence of the electric field on the streaks has been reported in Soldati & Banerjee (1998). These authors reported that the spanwise spacing of the low-speed streaks is approximately 105 ± 15 in wall units, which is different from the average spanwise spacing of the streaks in Poiseuille flow, which is 100 in wall units (see e.g. Butler & Farrell 1993). Thus, to some extent, our results that the spanwise spacing of the streaks changes in the linear EHD cross-flow agree qualitatively with these findings. These authors also found that the cross-flow is weakened by the electric field. This does not stand in conflict with the current results, because enhanced transient growth due to the electric field, as found here, only indicates that, in the linear phase, transition to turbulence is more rapid when compared to canonical channel flow; no conclusions can be drawn for the flow behaviour in the nonlinear regime. To more fully understand how the electric field influences streaks and streamwise vortices in the nonlinear phase of transition, a more comprehensive study of the role played by EHD in the formation and dynamics of a self-sustaining cycle (Jiménez & Pinelli 1999) is called for.

To further investigate the effect of T, we plot in figure 10 the optimal initial conditions that achieve G_{max} in a given finite time for parameters $C = 100$, $Re = 5000$, $Fe = 10^5$, $\alpha = 0$ and different values of T with its corresponding optimal β. In figure 10(*a*), the optimal initial conditions for v for various T are presented. The symmetry of the optimal v with respect to the flow centreline $y = 0$, when the flow is close to the pure-hydrodynamics limit, is broken due to the action of the electric field in the wall-normal direction as T increases. Since the electrode with higher potential is at $y = 1$ in our case, the optimal initial conditions for w and v are tilted towards $y = 1$ (see also figure 10(*b*), which additionally shows the optimal initial condition for φ). In figure 10(*c*), the formation of streamwise vortices in the y–z plane is shown; their centres are shifted upwards by the electric field. In figure 10(*d*), the optimal response of φ, taking the form of waves in the spanwise direction, is displayed. Recalling that the non-modal transient growth is due to base-flow modulations arising from the tilting of spanwise into wall-normal vorticity, we can state that the variation of the optimal spanwise wavenumber for different T is the direct result of the three-dimensional nature of the non-normal linearized operator under the influence of a constant electric field pointing in the wall-normal coordinate direction.

5. Results of energy analysis

5.1. *Asymptotic energy analysis*

The dynamics of the disturbance energy (of the velocity fluctuations) in the limit of an infinite time horizon is examined in this section. The governing equation for the energy evolution is obtained by multiplying the linearized equation (2.8*b*) by the complex conjugate velocity $v_i^\dagger$, i.e.

$$v_i^\dagger \frac{\partial v_i}{\partial t} + v_i^\dagger v_j \frac{\partial \bar{U}_i}{\partial x_j} + v_i^\dagger \bar{U}_j \frac{\partial v_i}{\partial x_j} = -v_i^\dagger \frac{\partial p}{\partial v_i} + v_i^\dagger \frac{M^2}{T} \frac{\partial^2 v_i}{\partial x_j^2} + v_i^\dagger M^2 \left(\frac{\partial \bar{\phi}}{\partial x_i} \frac{\partial^2 \varphi}{\partial x_j x_j} + \frac{\partial^2 \bar{\phi}}{\partial x_j x_j} \frac{\partial \varphi}{\partial x_i} \right), \tag{5.1}$$

https://doi.org/10.1017/jfm.2015.134 Published online by Cambridge University Press

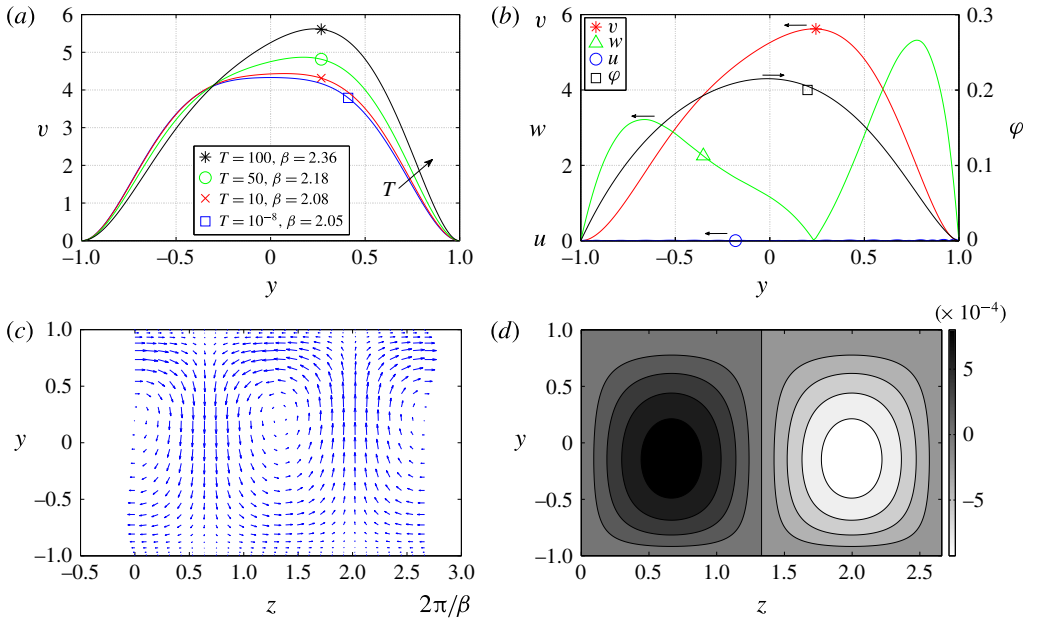


FIGURE 10. (Colour online) Effect of T. (*a*) The optimal initial condition for v as a function of T and β at $C = 100$, $Fe = 10^5$, $Re = 5000$ and $\alpha = 0$. (*b*) The optimal initial conditions for velocity and potential at $C = 100$, $Re = 5000$, $Fe = 10^5$, $T = 100$, $\alpha = 0$ and $\beta = 2.36$. (*c*) Velocity vectors of the optimal initial condition in the cross-stream plane; same parameters as in panel (*b*). (*d*) Contours of the optimal response for φ; same parameters as in panel (*b*).

taking the complex conjugate of the obtained equation, and averaging the two equations, which leaves us with

$$\begin{aligned}\frac{\partial \mathcal{E}}{\partial t} = & -\frac{1}{2}(v_i^\dagger v_j + v_j^\dagger v_i)\frac{\partial \bar{U}_i}{\partial x_j} - \frac{M^2}{T}\frac{\partial v_i^\dagger}{\partial x_j}\frac{\partial v_i}{\partial x_j} - \frac{M^2}{2}\frac{\partial \bar{\phi}}{\partial x_i}\left(\frac{\partial \varphi^\dagger}{\partial x_j}\frac{\partial v_i}{\partial x_j} + \frac{\partial \varphi}{\partial x_j}\frac{\partial v_i^\dagger}{\partial x_j}\right) \\ & - \frac{M^2}{2}\frac{\partial^2 \bar{\phi}}{\partial x_i \partial x_j}\left(v_i^\dagger \frac{\partial \varphi}{\partial x_j} + v_i \frac{\partial \varphi^\dagger}{\partial x_j}\right) - \frac{M^2}{2}\frac{\partial^3 \bar{\phi}}{\partial x_i \partial x_i \partial x_j}(\varphi v_j^\dagger + \varphi^\dagger v_j) \\ & + \frac{\partial}{\partial x_j}\left[-\frac{1}{2}v_i v_i^\dagger \bar{U}_j - \frac{1}{2}(v_i^\dagger p + v_i p^\dagger)\delta_{ij} + \frac{M^2}{2T}\left(v_i^\dagger \frac{\partial v_i}{\partial x_j} + v_i \frac{\partial v_i^\dagger}{\partial x_j}\right)\right. \\ & \left. + \frac{M^2}{2}\frac{\partial \bar{\phi}}{\partial x_i}\left(\frac{\partial \varphi}{\partial x_j}v_i^\dagger + \frac{\partial \varphi^\dagger}{\partial x_j}v_i\right) + \frac{M^2}{2}\frac{\partial^2 \bar{\phi}}{\partial x_i x_i}\left(\varphi v_j^\dagger + \varphi^\dagger v_j\right)\right], \end{aligned} \tag{5.2}$$

where $\mathcal{E} = v_i^\dagger v_i/2$ is the perturbation energy density of the hydrodynamic part of the spectral space. The terms in the square brackets are the transport terms, which, in the case of periodic as well as no-slip and no-penetration boundary conditions, exert no influence on the energy balance. Therefore, after integrating the above equation over

https://doi.org/10.1017/jfm.2015.134 Published online by Cambridge University Press

the control volume Ω, we obtain

$$\begin{aligned}\int_\Omega \frac{\partial \mathcal{E}}{\partial t}\mathrm{d}V = &\underbrace{-\int_\Omega \frac{1}{2}(v_i^\dagger v_j + v_j^\dagger v_i)\frac{\partial \bar{U}_i}{\partial x_j}\mathrm{d}V}_{\mathsf{Pr}} \underbrace{-\int_\Omega \frac{M^2}{T}\frac{\partial v_i^\dagger}{\partial x_j}\frac{\partial v_i}{\partial x_j}\mathrm{d}V}_{\mathsf{VD}} \\ &\underbrace{-\int_\Omega \frac{M^2}{2}\frac{\partial \bar{\phi}}{\partial x_i}\left(\frac{\partial \varphi^\dagger}{\partial x_j}\frac{\partial v_i}{\partial x_j}+\frac{\partial \varphi}{\partial x_j}\frac{\partial v_i^\dagger}{\partial x_j}\right)\mathrm{d}V}_{\mathsf{VE1}} \\ &\underbrace{-\int_\Omega \frac{M^2}{2}\frac{\partial^2 \bar{\phi}}{\partial x_i \partial x_j}\left(v_i^\dagger \frac{\partial \varphi}{\partial x_j}+v_i\frac{\partial \varphi^\dagger}{\partial x_j}\right)\mathrm{d}V}_{\mathsf{VE2}} \\ &\underbrace{-\int_\Omega \frac{M^2}{2}\frac{\partial^3 \bar{\phi}}{\partial x_i \partial x_i \partial x_j}(\varphi v_j^\dagger + \varphi^\dagger v_j)\mathrm{d}V}_{\mathsf{VE3}}. \end{aligned} \tag{5.3}$$

Since the boundary conditions are periodic in the wall-parallel coordinate directions, it is legitimate to consider the control 'volume' Ω in only the y direction, that is, $\Omega = [-1, 1]$ and $\mathrm{d}V = \mathrm{d}y$. The first term on the right-hand side of (5.3) represents energy production from the mean shear (Pr), which is zero in the hydrostatic case; the second term describes viscous dissipation (VD); the third to fifth terms are the energy transfer terms between the velocity fluctuation field and the electric field (VE1, VE2 and VE3, respectively). The Einstein summation convention does not apply for the subscripts of $\mathsf{VE1}_{ij}$; the term $\mathsf{VE1}_{21}$, for example, represents $\int_\Omega (M^2/2)(\partial\bar{\phi}/\partial y)[(\partial\varphi^\dagger/\partial x)(\partial v/\partial x) + (\partial\varphi/\partial x)(\partial v^\dagger/\partial x)]\mathrm{d}V$.

As has been discussed and verified for polymeric flows in Zhang *et al.* (2013), the time variation of the normalized perturbation energy density R_e should be equal to twice the asymptotic growth rate of linear disturbances, i.e.

$$R_e = \frac{\displaystyle\int_\Omega \frac{\partial \mathcal{E}}{\partial t}\mathrm{d}V}{\displaystyle\int_\Omega \mathcal{E}\mathrm{d}V} = 2\omega_i, \tag{5.4}$$

where ω_i denotes the growth rate of the least stable mode. We will validate this relation in the following sections and use it as an *a posteriori* check for our results.

5.1.1. *Electrohydrodynamics without cross-flow*

We apply the energy analysis for hydrostatic EHD flow with different values of charge diffusion coefficients Fe to probe how the electric field interacts with the velocity fluctuations. Quantitative results are listed in table 1, with the notation $\mathsf{VD} = \mathsf{VD}_{11} + \mathsf{VD}_{12} + \mathsf{VD}_{21} + \mathsf{VD}_{22}$ and, likewise, $\mathsf{VE} = \mathsf{VE1}_{21} + \mathsf{VE1}_{22} + \mathsf{VE2} + \mathsf{VE3}$. There is no spanwise dependence, as $\beta = 0$. Immediately, one can make several direct observations. First, viscous dissipation is always negative for the hydrodynamics. Secondly, since the EHD flow is hydrostatic, there is no production from the mean shear, $\mathsf{Pr} = 0$. The only terms that can lead to growth in the hydrodynamic disturbance energy density $\mathcal{E}$ are linked to the energy transfer from the electric field, VE. The most efficient mechanism seems to be related to the term $\mathsf{VE1}_{21}$, which represents

https://doi.org/10.1017/jfm.2015.134 Published online by Cambridge University Press

Terms	$Fe = 10^4$	$Fe = 10^5$	$Fe = 10^6$	$Fe = 10^7$
VD_{11}	−254.9836	−255.3751	−255.4628	−255.4781
VD_{12}	−481.9379	−486.1119	−487.0231	−487.1773
VD_{21}	−570.6289	−570.2374	−570.1497	−570.1344
VD_{22}	−254.9836	−255.3751	−255.4628	−255.4781
$\mathsf{VE1}_{21}$	1154.1206	1152.8793	1152.6403	1152.5936
$\mathsf{VE1}_{22}$	428.695	431.8134	432.4984	432.6197
VE2	30.0141	30.7628	30.9299	30.9614
VE3	−50.2196	−48.3506	−47.9797	−47.9186
VD	−1562.5341	−1567.0994	−1568.0984	−1568.2679
VE	1562.6102	1567.1049	1568.089	1568.2561
Pr	0	0	0	0
R_e	0.0761	0.0054	−0.0094	−0.0119
$2\omega_i$	0.0761	0.0054	−0.0094	−0.0119

TABLE 1. Energy budget for modal instability of hydrostatic EHD flow for different values of the charge diffusion. The results are normalized as in (5.4). The parameters are $C = 50$, $M = 100$, $T = 160$, $\alpha = 2.57$ and $\beta = 0$ for hydrostatic flow.

the interaction between the streamwise perturbed electric field and the wall-normal velocity shear under the constant effect of the wall-normal base electric field. The term VE3 is even negative, indicating that the electric field can absorb energy from the perturbed hydrodynamic field by an out-of-phase configuration between φ and v (in the energy-budget equation for the perturbed electric field, one would find exactly the same term with opposite sign). Regarding the effect of charge diffusion, with increasing $1/Fe$ (increasing charge diffusion) from the right column to the left in table 1, the total energy transfer VE diminishes, but, at the same time, the hydrodynamic diffusion is also dissipating less energy into heat. Furthermore, even though VE (and thus $\mathsf{VE1}_{22}$, VE2 and VE3) decreases with rising charge diffusion, the primary mechanism of energy transfer $\mathsf{VE1}_{21}$ transfers more energy from the electric field to the hydrodynamic fluctuations, together with less dissipation, leading to an unstable flow for the chosen parameters. Therefore, it seems that the effect of charge diffusion is to catalytically enhance the efficiency of the most productive energy transfer mechanism between the perturbed electric field and the hydrodynamics, expressed by the term $\mathsf{VE1}_{21}$, resulting in a lower dissipation. As a consequence, increasing charge diffusion leads to a more unstable flow.

It is instructive to assess the effect of M on the linear stability (see § 4.1) with the help of the energy-budget equation (5.3). For a vanishing time derivative of the energy density, the factor M^2 on the right-hand side can be eliminated for the hydrostatic case $\bar{U} = 0$. In the case of cross-flow, however, by the same reasoning M will have an influence on the linear stability criterion.

5.1.2. *Electrohydrodynamics with low-Re cross-flow*

Table 2 shows the results for $C = 50$, $M = 100$, $T = 160$, $Re = T/M^2 = 0.016$, $\alpha = 2.57$ and $\beta = 0$ with cross-flow for different Fe. Compared to the case without cross-flow, the results are quite similar. However, it is interesting to note that the

https://doi.org/10.1017/jfm.2015.134 Published online by Cambridge University Press

Terms	$Fe = 10^4$	$Fe = 10^5$	$Fe = 10^6$	$Fe = 10^7$
VD_{11}	−254.1325	−254.1337	−254.1318	−254.1309
VD_{12}	−475.0779	−476.292	−476.5068	−476.5348
VD_{21}	−571.48	−571.4788	−571.4807	−571.4816
VD_{22}	−254.1325	−254.1337	−254.1318	−254.1309
$\mathsf{VE1}_{21}$	1158.7772	1157.62	1157.3579	1157.3025
$\mathsf{VE1}_{22}$	422.786	423.6012	423.7687	423.7989
VE2	26.3245	26.363	26.3747	26.3794
VE3	−52.8799	−51.3981	−51.1094	−51.0629
VD	−1554.8229	−1556.0382	−1556.2511	−1556.2782
VE	1555.0078	1556.1861	1556.3919	1556.4179
Pr	−0.0079038	−0.0080187	−0.0080507	−0.0080566
R_e	0.1769	0.1399	0.1327	0.1316
$2\omega_i$	0.1769	0.1399	0.1327	0.1316

TABLE 2. Energy budget for modal instability of EHD flow with low-Re cross-flow for different values of the charge diffusion Fe. The results are normalized as in (5.4). The parameters are $C = 50$, $M = 100$, $T = 160$, $Re = T/M^2 = 0.016$, $\alpha = 2.57$ and $\beta = 0$ with cross-flow.

fluctuation energy production from the mean shear Pr, even though rather small, is negative, indicating that the perturbed flow field transfers energy to the base flow. Recalling the results in figure 7 of § 4.2.1, a change of M does not have a strong effect on the rate of change of the disturbance energy density $\mathcal{E}$ since Pr is very small.

In the case of EHD flow with a weak cross-flow ($Re = 0.016$), the main mechanism for transferring energy into the hydrodynamic subsystem is still based on the potential difference across the two electrodes – the same as for the no cross-flow case. This can be confirmed by inspecting table 2: $\mathsf{VE1}_{21}$ is the dominant energy transfer term.

5.1.3. *Electrohydrodynamics with high-Re cross-flow*

The energy analysis for the EHD Poiseuille flow at $C = 100$, $Fe = 10^5$, $Re = 5500$, $\alpha = 1$ and $\beta = 0$ is summarized in table 3. Note that the production Pr is diminishing with increasing T. On the other hand, VE increases with larger values of T, compensating and exceeding the decrease of Pr at higher T. This is consistent with the results in figure 8: higher values of T yield a more unstable flow. However, the principal mechanism underlying the flow instability is still linked to the production Pr. The electric field only assumes a secondary role in destabilizing the flow, at least for the parameters considered in this case. Unlike the hydrostatic case where $\mathsf{VE1}_{21}$ is responsible for the dominant energy transfer, in the presence of cross-flow $\mathsf{VE1}_{22}$ becomes the most efficient agent transferring fluctuation energy $\mathcal{E}$ between the electric field and the perturbed velocity field.

5.2. *Transient energy analysis*

To investigate the cause for the increase of non-modal growth with T (recall figure 9), we formulate and perform an energy analysis for the initial-value problem of (2.16). We consider the energy density evolution over a finite time horizon following

https://doi.org/10.1017/jfm.2015.134 Published online by Cambridge University Press

Terms ($\times 10^{-4}$)	$T = 10^{-8}$	$T = 10$	$T = 100$	$T = 200$
VD_{11}	-2.643	-2.643	-2.6429	-2.6429
VD_{12}	-138.22	-138.24	-138.42	-138.61
VD_{21}	-0.99338	-0.99339	-0.99343	-0.99347
VD_{22}	-2.643	-2.643	-2.6429	-2.6429
$\mathsf{VE1}_{21}$	3.1782×10^{-10}	0.31785	3.1814	6.3689
$\mathsf{VE1}_{22}$	7.3458×10^{-10}	0.73467	7.355	14.729
VE2	7.0501×10^{-11}	0.070507	0.70555	1.4122
VE3	-1.2043×10^{-10}	-0.12044	-1.2055	-2.4133
VD	-144.5	-144.52	-144.7	-144.89
VE	10.025×10^{-10}	1.0026	10.036	20.096
Pr	132.35	132.06	129.41	126.44
R_e	-12.153	-11.463	-5.2526	1.6542
$2\omega_i$	-12.153	-11.463	-5.2526	1.6542

TABLE 3. Energy budget for modal instability of EHD flow with a high-Re cross-flow for different values of the stability parameter T. The results are normalized as in (5.4). The parameters are $C = 100$, $Fe = 10^5$, $Re = 5500$, $\alpha = 1$ and $\beta = 0$ with cross-flow.

Butler & Farrell (1992),

$$\frac{1}{|\Omega|}\int_{\Omega}\frac{\partial \mathcal{E}}{\partial t}\mathrm{d}V = \frac{1}{|\Omega|}\int_{-1}^{1}\int_{0}^{a}\int_{0}^{b}\frac{\partial}{\partial t}\left(\frac{u^2+v^2+w^2}{2}\right)\mathrm{d}V$$
$$= \frac{1}{|\Omega|}\int_{-1}^{1}\int_{0}^{a}\int_{0}^{b}\Bigg[\underbrace{-uv\frac{\mathrm{d}U}{\mathrm{d}y}}_{\mathsf{Pr}} - \underbrace{\frac{1}{Re}\frac{\partial u_i}{\partial x_j}\frac{\partial u_i}{\partial x_j}}_{\mathsf{VD}}$$
$$\underbrace{-\frac{T}{Re}\frac{\partial \bar{\phi}}{\partial y}\frac{\partial \varphi}{\partial x_j}\frac{\partial v}{\partial x_j}}_{\mathsf{VE1}} \underbrace{-\frac{T}{Re}\frac{\partial^2 \bar{\phi}}{\partial y^2}v\frac{\partial \varphi}{\partial y}}_{\mathsf{VE2}} \underbrace{-\frac{T}{Re}\frac{\partial^3 \bar{\phi}}{\partial y^3}\varphi v}_{\mathsf{VE3}}\Bigg]\mathrm{d}z\mathrm{d}x\mathrm{d}y, \quad (5.5)$$

where $|\Omega| = 2ab$, $a = 2\pi/\alpha$ and $b = 2\pi/\beta$. In the above equation, we label, as before, the first term on the right-hand side as Pr (production from the mean shear), the second term as VD (viscous dissipation), the third to fifth terms collectively as VE (energy density transfer between the perturbed velocity field and the perturbed electric field) and the sum of all five terms as Total. In this temporal evolution problem, the initial condition is the optimal one, following the procedure in § 4.2.2.

The results of our energy analysis are presented in figure 11. In panel (*a*) and its inset, the pure hydrodynamic result is shown, where the production Pr counteracts the viscous dissipation VD. In panel (*b*) for EHD cross-flow, we observe that the term VE is insignificant, even though at $T = 100$; this is in contrast to both the linear modal stability criterion (see figure 8) and the overall non-modal transient growth (see figures 9 and 10), where its effect is not negligible. Furthermore, production Pr increases by a factor of 2–3 compared to the pure hydrodynamic flow. These results seem to indicate that, concerning the non-modal analysis, the effect of the additional electric field on the canonical channel flow is incidental, i.e. the perturbation velocity

https://doi.org/10.1017/jfm.2015.134 Published online by Cambridge University Press

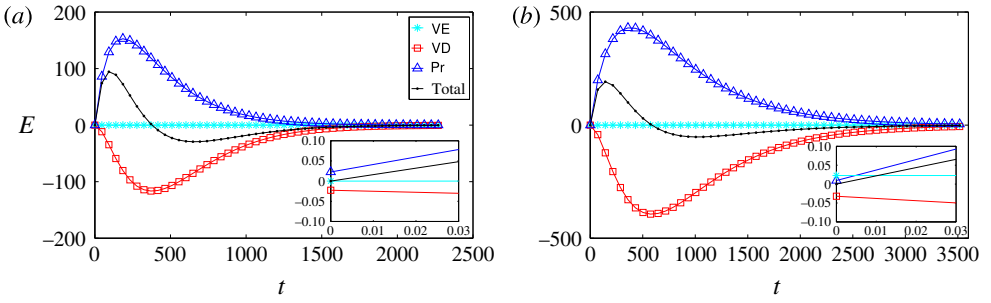


FIGURE 11. (Colour online) Energy analysis over a finite time horizon at $C = 100$, $Re = 5000$, $Fe = 10^5$ and $\alpha = 0$ for: (*a*) $T = 10^{-8}$ and $\beta = 2.05$; and (*b*) $T = 100$ and $\beta = 2.36$.

energy is only indirectly influenced by the electric field; in fact, the electric field does not induce a substantial energy transfer directly into velocity fluctuations at all and its effect is to enhance the lift-up mechanism, and therefore the production.

Examining more closely the inset in figure 11(*b*), we see that the term VE surpasses Pr only at the very beginning of the time horizon. This is due to the high-*Re* regime we are investigating. As discussed earlier, $Re = T/M^2$ represents the ratio of the momentum relaxation time L^{*2}/ν^* to the charge relaxation time $L^{*2}/(K^*\Delta\phi_0^*)$. With the maximum Total energy achieved at $t_{max} \approx 144$ in figure 11(*b*), we can estimate the time horizon in the inset by observing that $144/5000 = 0.029$, a value close to the time scale depicted in the inset of panel (*b*). Moreover, the minimal energy growth due to the electric force validates our previous observation that the purely EHD-induced non-normality is rather small (see appendix B for a direct proof of this statement via an input–output formulation). In the case of other complex flows at high Reynolds numbers, a similar conclusion can be drawn; for instance, in viscoelastic flows (Zhang *et al.* 2013; Brandt 2014), polymer stretching cannot induce disturbance growth when the fluid inertia is prevalent.

6. Discussion and conclusions

In this article, we have presented a comprehensive linear stability analysis of charge-injection-induced EHD flows between two plate electrodes, covering the hydrostatic as well as the cross-flow case, employing modal as well as non-modal tools. We intend to examine whether the linear framework is sufficient for describing the transition to turbulence of EHD flow in the early phase of perturbation evolution. It is hoped that the results presented above and summarized below would help to understand better the EHD flow instability and its transition mechanism and shed light on its flow physics as well as flow control design.

6.1. *Electrohydrodynamics without cross-flow*

In the hydrostatic case, the often-omitted charge diffusion is taken into account and found to have a non-negligible effect, particularly on the critical linear stability parameter T_c with SCL injection – a finding running contrary to a common assumption in previous studies. In those studies, a linear stability analysis predicts a critical value of $T_c \approx 161$ in the strong-injection limit. This result is reproduced in our computations for a negligible value of $1/Fe$, but even for a moderate amount of charge diffusion

https://doi.org/10.1017/jfm.2015.134 Published online by Cambridge University Press

the flow quickly becomes more unstable. Hence, we suggest that charge diffusion be accounted for in linear stability analyses and numerical simulations whenever the real physics indicates charge diffusion that cannot be neglected, as it improves not only the model of the flow physics but also the robustness of the numerics as well. In fact, the common use of total variation diminishing (TVD) schemes (Harten 1983) in direct numerical simulations of EHD flow, which introduces artificial numerical diffusion, seems unnecessary when true physical charge diffusion could be included.

The longstanding discrepancy of the critical stability parameter T_c between the experimental and theoretical values, however, could not be resolved by our analysis: even though T_c in the SCL limit drops to 140 at $Fe = 10^3$ (a physical value according to Pérez & Castellanos (1989)), a substantial gap remains to the experimentally measured parameter of $T_c \approx 110$. Motivated by research in subcritical channel flow, we examine other mechanisms for early transition to turbulence, specifically, transient growth due to the non-normality of the linearized EHD operator. Non-modal stability theory has been successfully applied to the variety of wall-bounded shear flows in an attempt to explain aspects of the transition process. In the case of hydrostatic EHD flow, our calculations seem to indicate that transient energy growth, as defined in (2.19), is not significant, reaching gains of $\sim$10 at most: rather, the flow instability is dictated by the asymptotic growth rate of the least stable mode. These results seem to indicate that below the critical T_c the significant energy growth observed in real EHD flow is not of a linear nature, otherwise the linear framework would succeed in detecting it. It might be hypothesized that the major energy growth mechanism in subcritical hydrostatic EHD follows a nonlinear route; nevertheless, it is only after performing a full nonlinear simulation of subcritical EHD flow that can one conclude whether its energy growth mechanism is truly nonlinear or not. Besides, these results also seem to shed some light on the flow control of hydrostatic EHD. It is now well established that, in canonical channel flow, where the perturbation energy is found to grow linearly in the early phase, a linear flow control strategy is sufficient to abate the perturbation development (Kim 2003; Kim & Bewley 2007). Owing to the limited early perturbation energy growth in hydrostatic EHD, we thus suggest that different flow control methods be examined and applied in addressing the flow control of such flow. There might exist another possibility for the limited transient growth. As discussed by Atten (1974), the correct prediction of the linear stability criterion might require a closer comparison between the experimental conditions and the mathematical model. In light of this, one may suggest a re-examination of the charge creation and transport processes, as the current charge creation model does not seem to accommodate any efficient energy transfer from the electric to the flow field, during the linear phase.

6.2. *Electrohydrodynamics with cross-flow*

The flow instability and the transition to turbulence in canonical or complex channel (for example, EHD, MHD or polymeric) flows are currently not well understood. The study of complex channel flow, serving as a supplement to the investigation of canonical flows, focuses on the flow modification under the influence of external fields, for example, electric field, magnetic field or polymer stress field. The study of such flows will not only improve our understanding of these particular flow configurations, but also, more importantly, help us to better understand, during the linear, transition and turbulent phases, the dynamics of the important flow structures, for instance, streak formation and attenuation, by probing the interaction between the fluids (or

https://doi.org/10.1017/jfm.2015.134 Published online by Cambridge University Press

flow structures) and the external fields. For example, from the point of view of flow control, research on polymer turbulence drag reduction reveals the mechanism of how the auto-generation cycles of turbulence are modified in the presence of polymer molecules (Dubief *et al.* 2004). This has led to an even broader picture of the dynamics of turbulence. Similarly, in the case of EHD, our goal is to understand how the flow changes in response to the electric effects and to provide a physical interpretation. Below we present the results of EHD cross-flow. We differentiated low-*Re* and high-*Re* cases. For low-*Re* flow, the effects of M and Fe are similar to those of the hydrostatic flow, with the linear stability criterion being smaller for low-*Re* cross-flow when compared to hydrostatic flow.

The high-*Re* case is more interesting. In both modal and non-modal stability analyses, the canonical channel flow becomes more unstable, once an electric field is applied between the two electrodes. From an input–output and an energy analysis, we found, however, that energy growth directly related to the electric field is not significant and that the effect of the electric field on the flow instability is indirect. In general, in high-*Re* channel flow, the maximum transient growth is achieved by vortices aligning along the streamwise coordinate direction and generating streamwise streaks via an efficient energy growth mechanism known as lift-up. These optimal streamwise vortices are symmetric with respect to the channel centreline for standard Poiseuille flow. In contrast to other complex flows, in EHD flows the electric field, which always points in the wall-normal direction, actively participates in the formation of the streamwise rolls by accelerating the downward-moving fluid (note that, in our setting, the injector is at $y = 1$). Consequently, this yields stronger transient growth via the lift-up mechanism, when compared to the common channel flow. In other words, the electric field provides wall-normal momentum. As has been discussed in Landahl (1980) and recently reviewed by Brandt (2014), the presence of wall-normal momentum will cause any three-dimensional, asymptotically stable or unstable shear flow to exhibit energy growth during a transient phase. In the present study, the role of the electric field is to provide the shear flow with such a source of wall-normal momentum and to strengthen the lift-up mechanism for EHD flow with high-*Re* cross-flow. Besides, we also find that the optimal wavenumbers for maximum transient growth increase under a stronger electric effect. Since the electric field will help to establish streamwise vortices, it may constitute a good actuator for drag reduction techniques, using the two-dimensional rolls together with a flow control strategy as described in Schoppa & Hussain (1998) and Soldati & Banerjee (1998).

Acknowledgements

F.M. was supported by the Italian Ministry for University and Research under grant PRIN 2010. The authors would like to thank Emanuele Bezzecchi for his initial input. M.Z. would like to thank Professor Luca Brandt of the Royal Institute of Technology (KTH), Sweden, and Dr P. Jordan of Université de Poitiers, France.

Appendix A. Code validation

We first perform a resolution check to examine the convergence of the results. The parameters in this case are $C = 50$, $Fe = 2000$, $Re = 6000$, $T = 100$, $M = \sqrt{T/Re} = 0.129$, $\alpha = 1$ and $\beta = 0$. The eigenspectra for four different grid resolutions N are shown in figure 12(*a*). The most unstable modes in these cases are listed in table 4. Satisfactory convergence, with increasing N, is observed.

https://doi.org/10.1017/jfm.2015.134 Published online by Cambridge University Press

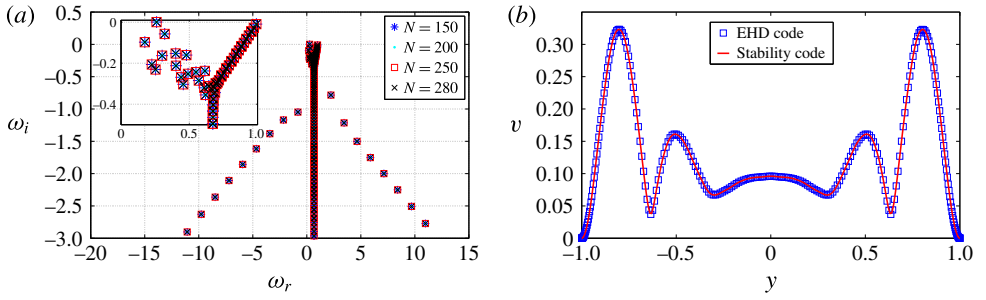


FIGURE 12. (Colour online) Code validation. (*a*) Resolution check for EHD flow with cross-flow at $C = 50$, $Fe = 2000$, $Re = 6000$, $T = 100$, $M = \sqrt{T/Re} = 0.1291$, $\alpha = 1$ and $\beta = 0$. (*b*) Eigenvector component v for the most unstable mode (normalized to have the same peak value for the two codes). The parameters are $C = 50$, $M = 10^{-11}$, $Fe = 2000$, $Re = 6000$, $T = M^2\,Re$, $\alpha = 1$, $\beta = 0$ and $N = 250$ for the EHD code; and $Re = 6000$, $\alpha = 1$, $\beta = 0$ and $N = 250$ for the hydrodynamic stability code.

N	Most unstable mode
150	0.260023637950300 + 0.000652797815269i
200	0.260023637089882 + 0.000652796819289i
250	0.260023637069851 + 0.000652796791624i
280	0.260023637052960 + 0.000652796810920i

TABLE 4. Code validation. Resolution check for the most unstable eigenvalue of EHD flow with cross-flow; with the same parameters as in figure 12.

Secondly, the EHD eigenvector, using (3.1), is examined against a verified, pure hydrodynamic stability code employing the same spectral collocation method and solving the Orr–Sommerfeld–Squire system (see Schmid & Henningson 2001), as shown in figure 12(*b*). The parameters for the EHD code are $C = 50$, $M = 10^{-11}$, $Fe = 2000$, $Re = 6000$, $T = M^2\,Re$, $\alpha = 1$, $\beta = 0$ and $N = 250$. The parameters for the hydrodynamic stability code are $Re = 6000$, $\alpha = 1$, $\beta = 0$ and $N = 250$. We see that the iteratively solved EHD eigenvector is the same as the pure hydrodynamic one, which is solved directly by the MATLAB routine `eig`. For the computation of the transient amplification G in (2.23), it is legitimate to include only the first several, most unstable modes (Schmid & Henningson 2001), i.e. eigenmodes corresponding to eigenvalues with imaginary part smaller than a certain ω_i^c are discarded (see table 5 for a validation of this approach). The reason for a minor increase of G, as more modes are included, is due to the newly incorporated eigenvectors, not because of an insufficiently refined grid.

With the eigenvalue problem reliably solved as shown above, we present validation for the specific flows considered here. In the case of hydrostatic flow, our results for $Fe = 10^7$, approximating the case of zero charge diffusion, $T_c = 160.67$ and $\alpha = 2.57$ at $C = 50$ (see figure 3*a* in § 4.1), are very close to the linear stability criterion reported in Atten & Moreau (1972), $T_c = 160.75$ and $\alpha = 2.569$ in the case of $C \to \infty$, where a coupled flow and electric system with neglected charge diffusion has been considered. This additionally implies that a value of C higher than 50 can well approximate the space-charge limit.

https://doi.org/10.1017/jfm.2015.134 Published online by Cambridge University Press

ω_i^c	G	ω_i^c	$G\,(\times 10^4)$
−3.5	3.312404	−0.5	1.138543
−5.5	3.434333	−3.5	1.174459
−7.5	3.434351	−10.5	1.175565

TABLE 5. Values of G versus different cutoff growth rates ω_i^c. The first two columns represent hydrostatic EHD flow at $C = 50$, $Fe = 10^5$, $M = 100$, $T = 155$, $\alpha = 2.5$, $\beta = 0$ and $N = 250$. The last two columns represent EHD flow with cross-flow at $C = 100$, $Fe = 10^5$, $Re = 5000$, $T = 100$, $\alpha = 0$, $\beta = 2.36$ and $N = 250$. Refer to the text for the definition of ω_i^c.

	EHD code	Hydrodynamic stability code
$\omega_{max,r}$	0.259815871017297	0.259815871062631
$\omega_{max,i}$	0.000323088678313	0.000323088655527
t_{max}	18.86745	18.87514
G_{max}	38.92401	38.93307

TABLE 6. Code validation. The parameters are the same as in figure 13.

In the presence of cross-flow, since there exist no quantitative results for eigenvalues and eigenvectors of the EHD problem in the literature, we partially verify our results by examining the pure hydrodynamic limit of the EHD linearized problem, i.e. with electric effects being very small. This comparison is made with the stability code. The parameters are identical to the ones chosen above for the comparison of the eigenvectors. The Poiseuille base flow is $\bar{U} = 1 - y^2$ in both codes. It is obvious that, with these selected parameters, the governing equation (2.13*c*) for φ is void of the coupling with v, since $\boldsymbol{L}_{v\varphi}$ in (2.15) is negligible. Therefore, the hydrodynamic equations for v and η in (2.13*a*) and (2.13*b*) must reproduce the results of the stability code. This match is shown in figure 13. In panel (*a*), the spectra of the two codes are seen to collapse, even in the intersection region of the three eigenbranches, which is known to be sensitive due to the high non-normality of the linearized system (Schmid & Henningson 2001). Additionally, the eigenmodes (blue squares) in panel (*a*) not matched by the hydrodynamic modes (red asterisks) are the supplementary eigenvalues linked to the presence of an electric field. The most unstable eigenvalue is shown in table 6. In panel (*b*), transient growth using an eigenvector expansion with $n = 71$ eigenmodes is shown. A quantitative comparison of the maximum transient growth G_{max} and its corresponding time t_{max} is presented in table 6. Agreement up to the fourth digit is achieved. The computations of t_{max} and G_{max} involve $n = 71$ eigenfunctions, each one solved with the iterative method. Even though each individual mode may be prone to small inaccuracies, figure 13(*b*) illustrates that transient growth (a multi-modal phenomenon) can be reliably and robustly computed using the eigenvector expansion outlined above.

Appendix B. Input–output formulation

An input–output formulation can reveal additional information on prevalent instability mechanisms by considering different types of forcings (input) and responses (output) (Jovanović & Bamieh 2005). To demonstrate that the transient growth due

https://doi.org/10.1017/jfm.2015.134 Published online by Cambridge University Press

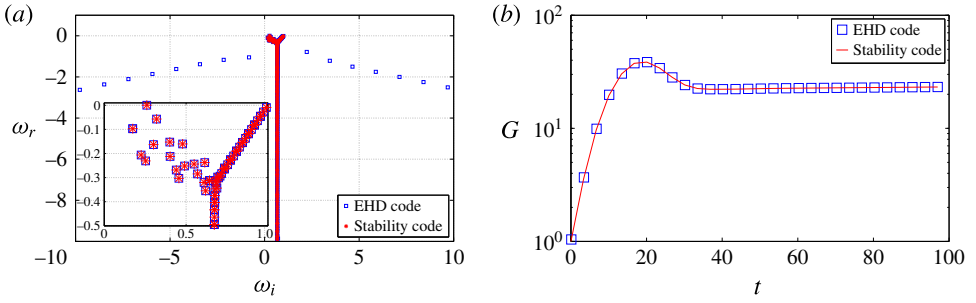


FIGURE 13. (Colour online) Comparison between EHD Poiseuille flow and canonical Poiseuille flow: (*a*) eigenvalue spectrum; and (*b*) transient amplification of initial energy. The parameters are $C = 50$, $M = 10^{-11}$, $Fe = 2000$, $Re = 6000$, $T = M^2\,Re$, $\alpha = 1$, $\beta = 0$ and $N = 250$ for the EHD code; and $Re = 6000$, $\alpha = 1$, $\beta = 0$ and $N = 250$ for the purely hydrodynamic stability code.

Input	$B_{in1}\{v, \eta, \varphi\}$	$B_{in2}\{v, \eta\}$	$B_{in3}\{\varphi\}$
t_{max}	583.4087	587.7147	552.0443
G_{max}	11765.40	11350.38	428.8926

TABLE 7. Results from an input–output analysis at $C = 100$, $Fe = 10^5$, $Re = 5000$, $T = 100$, $\alpha = 0$ and $\beta = 2.36$.

to perturbative φ is small, we compare the full responses to perturbations consisting of (i) all variables v, η and φ, (ii) both v and η, and (iii) only φ. We thus define for these three cases different input filters $\boldsymbol{B}$, where $\boldsymbol{B}_{in1} = \boldsymbol{I}_{3N\times 3N}$ for the first case, while for the second and third cases we have

$$\boldsymbol{B}_{in2} = \begin{pmatrix} \boldsymbol{I}_{N\times N} & \boldsymbol{0} \\ \boldsymbol{0} & \boldsymbol{I}_{N\times N} \\ \boldsymbol{0} & \boldsymbol{0} \end{pmatrix}, \quad \boldsymbol{B}_{in3} = \begin{pmatrix} \boldsymbol{0} \\ \boldsymbol{0} \\ \boldsymbol{I}_{N\times N} \end{pmatrix}. \tag{B 1a,b}$$

The output filter $\boldsymbol{C}_{out}$ is $\boldsymbol{I}_{3N\times 3N}$ for all three cases: we examine the flow response in all velocities and the electric field. Consequently, the energy weight matrices should be redefined with $\boldsymbol{M}_{out} = \boldsymbol{C}_{out}\boldsymbol{M}\boldsymbol{C}_{out}^{\mathrm{T}}$ and $\boldsymbol{M}_{in} = \boldsymbol{B}_{in}^{\mathrm{T}}\boldsymbol{M}\boldsymbol{B}_{in}$. After applying a Cholesky decomposition to these energy weight matrices, we obtain $\boldsymbol{F}_{out}$ and $\boldsymbol{F}_{in}$ for a formulation based on the L_2-norm. Finally, the maximum transient growth G over a finite time interval is given by

$$\begin{aligned} G(t) &= \max_{\boldsymbol{\gamma}_0} \frac{\|\boldsymbol{\gamma}_{out}(t)\|_{E_{out}}}{\|\boldsymbol{\gamma}_{in}(0)\|_{E_{in}}} = \max_{\boldsymbol{\gamma}_0} \frac{\|\boldsymbol{\mathcal{T}}\boldsymbol{\gamma}_{in}(0)\|_{E_{out}}}{\|\boldsymbol{\gamma}_{in}(0)\|_{E_{in}}} = \max_{\boldsymbol{\gamma}_0} \frac{\|\boldsymbol{F}_{out}\boldsymbol{\mathcal{T}}\boldsymbol{\gamma}_{in}(0)\|_2}{\|\boldsymbol{F}_{in}\boldsymbol{\gamma}_{in}(0)\|_2} \\ &= \max_{\boldsymbol{\gamma}_0} \frac{\|\boldsymbol{F}_{out}\boldsymbol{\mathcal{T}}\boldsymbol{F}_{in}^{-1}\boldsymbol{F}_{in}\boldsymbol{\gamma}_{in}(0)\|_2}{\|\boldsymbol{F}_{in}\boldsymbol{\gamma}_{in}(0)\|_2} = \|\boldsymbol{F}_{out}\boldsymbol{\mathcal{T}}\boldsymbol{F}_{in}^{-1}\|_2 \\ &= \|\boldsymbol{F}_{out}\boldsymbol{C}_{out}\mathrm{e}^{t\boldsymbol{\mathcal{L}}}\boldsymbol{B}_{in}\boldsymbol{F}_{in}^{-1}\|_2. \end{aligned} \tag{B 2}$$

We report the transient growth results for the above three cases in table 7 at $C = 100$, $Fe = 10^5$, $Re = 5000$, $T = 100$, $\alpha = 0$ and $\beta = 2.36$. We observe that perturbations

https://doi.org/10.1017/jfm.2015.134 Published online by Cambridge University Press

solely in φ (case (iii)) exhibit transient growth two orders smaller than in the other two cases. For cases (i) and (ii) the transient growth characteristics are nearly identical, which suggests that the non-normality of the linear operator is mainly related to the hydrodynamics.

REFERENCES

ALJ, A., DENAT, A., GOSSE, J.-P., GOSSE, B. & NAKAMURA, I. 1985 Creation of charge carriers in nonpolar liquids. *IEEE Trans. Elec. Insul.* **20** (2), 221–231.

ALLEN, P. & KARAYIANNIS, T. 1995 Electrohydrodynamic enhancement of heat transfer and fluid flows. *Heat Recov. Syst. CHP* **15** (5), 389–423.

ATTEN, P. 1974 Electrohydrodynamic stability of dielectric liquids during transient regime of space-charge-limited injection. *Phys. Fluids* **17** (10), 1822–1827.

ATTEN, P. 1976 Rôle de la diffusion dans le problème de la stabilité hydrodynamique d'un liquide dièlectrique soumis à une injection unipolaire forte. *C. R. Acad. Sci. Paris* **283**, 29–32.

ATTEN, P. & HONDA, T. 1982 The electroviscous effect and its explanation I – The electrohydrodynamic origin; study under unipolar D.C. injection. *J. Electrostat.* **11** (3), 225–245.

ATTEN, P. & LACROIX, J. C. 1979 Non-linear hydrodynamic stability of liquids subjected to unipolar injection. *J. Méc.* **18**, 469–510.

ATTEN, P. & MOREAU, R. 1972 Stabilité electrohydrodynamique des liquides isolants soumis à une injection unipolaire. *J. Méc.* **11**, 471–520.

BART, S. F., TAVROW, L. S., MEHREGANY, M. & LANG, J. H. 1990 Microfabricated electrohydrodynamic pumps. *Sensors Actuators* A **21** (1–3), 193–197.

BOYD, J. 2001 *Chebyshev and Fourier Spectral Methods*, 2nd revised edn. Dover.

BRADSHAW, P. 1969 The analogy between streamline curvature and buoyancy in turbulent shear flow. *J. Fluid Mech.* **36**, 177–191.

BRANDT, L. 2014 The lift-up effect: the linear mechanism behind transition and turbulence in shear flows. *Eur. J. Mech. (*B*/Fluids)* **47**, 80–96.

BUSHNELL, D. M. & MCGINLEY, C. B. 1989 Turbulence control in wall flows. *Annu. Rev. Fluid Mech.* **21**, 1–20.

BUTLER, K. M. & FARRELL, B. F. 1992 Three-dimensional optimal perturbations in viscous shear flow. *Phys. Fluids* **4** (8), 1637–1650.

BUTLER, K. M. & FARRELL, B. F. 1993 Optimal perturbations and streak spacing in wall-bounded turbulent shear flows. *Phys. Fluids* A **5** (3), 774–777.

CASTELLANOS, A. 1998 *Electrohydrodynamics*. Springer.

CASTELLANOS, A. & AGRAIT, N. 1992 Unipolar injection induced instabilities in plane parallel flows. *IEEE Trans. Ind. Applics.* **28** (3), 513–519.

CHAKRABORTY, S., LIAO, I.-C., ADLER, A. & LEONG, K. W. 2009 Electrohydrodynamics: a facile technique to fabricate drug delivery systems. *Adv. Drug Deliv. Rev.* **61** (12), 1043–1054.

DARABI, J., RADA, M., OHADI, M. & LAWLER, J. 2002 Design, fabrication, and testing of an electrohydrodynamic ion-drag micropump. *J. Microelectromech. Syst.* **11** (6), 684–690.

DUBIEF, Y., WHITE, C. M., TERRAPON, V. E., SHAQFEH, E. S. G., MOIN, P. & LELE, S. K. 2004 On the coherent drag-reducing and turbulence-enhancing behaviour of polymers in wall flows. *J. Fluid Mech.* **514**, 271–280.

FARRELL, B. F. & IOANNOU, P. J. 1996 Generalized stability theory. Part I: autonomous operators. *J. Atmos. Sci.* **53** (14), 2025–2040.

FÉLICI, N. 1971 DC conduction in liquid dielectrics (Part II): electrohydrodynamic phenomena. *Direct Curr. Power Electron.* **2**, 147–165.

GROSSMANN, S. & LOHSE, D. 2000 Scaling in thermal convection: a unifying theory. *J. Fluid Mech.* **407**, 27–56.

HARTEN, A. 1983 High resolution schemes for hyperbolic conservation laws. *J. Comput. Phys.* **49** (3), 357–393.

https://doi.org/10.1017/jfm.2015.134 Published online by Cambridge University Press

JIMÉNEZ, J. & PINELLI, A. 1999 The autonomous cycle of near-wall turbulence. *J. Fluid Mech.* **389**, 335–359.

JONES, T. 1978 Electrohydrodynamically enhanced heat transfer in liquids – a review. *Adv. Heat Transfer* **14**, 107–148.

JOVANOVIĆ, M. R. & BAMIEH, B. 2005 Componentwise energy amplification in channel flows. *J. Fluid Mech.* **534**, 145–183.

KIM, J. 2003 Control of turbulent boundary layers. *Phys. Fluids* **15** (5), 1093–1105.

KIM, J. & BEWLEY, T. R. 2007 A linear systems approach to flow control. *Annu. Rev. Fluid Mech.* **39** (1), 383–417.

KOURMATZIS, A. & SHRIMPTON, J. S. 2012 Turbulent three-dimensional dielectric electrohydrodynamic convection between two plates. *J. Fluid Mech.* **696**, 228–262.

LACROIX, J. C., ATTEN, P. & HOPFINGER, E. J. 1975 Electro-convection in a dielectric liquid layer subjected to unipolar injection. *J. Fluid Mech.* **69**, 539–563.

LANDAHL, M. T. 1980 A note on an algebraic instability of inviscid parallel shear flows. *J. Fluid Mech.* **98**, 243–251.

LEE, J.-G., CHO, H.-J., HUH, N., KO, C., LEE, W.-C., JANG, Y.-H., LEE, B. S., KANG, I. S. & CHOI, J.-W. 2006 Electrohydrodynamic (EHD) dispensing of nanoliter DNA droplets for microarrays. *Biosens. Bioelectr.* **21** (12), 2240–2247.

MARTINELLI, F., QUADRIO, M. & SCHMID, P. J. 2011 Stability of planar shear flow in presence of electroconvection. In *Proceedings of the Seventh International Symposium on Turbulence and Shear Flow Phenomena (TSFP-7), July 2011, Ottawa, Canada*.

MELCHER, J. R. 1981 *Continuum Electromechanics*. MIT Press.

OGILVIE, G. I. & PROCTOR, M. R. E. 2003 On the relation between viscoelastic and magnetohydrodynamic flows and their instabilities. *J. Fluid Mech.* **476**, 389–409.

PÉREZ, A. T. & CASTELLANOS, A. 1989 Role of charge diffusion in finite-amplitude electroconvection. *Phys. Rev.* A **40**, 5844–5855.

SAAD, Y. 2011 *Numerical Methods for Large Eigenvalue Problems*. SIAM.

SCHMID, P. J. 2007 Nonmodal stability theory. *Annu. Rev. Fluid Mech.* **39**, 129–162.

SCHMID, P. J. & BRANDT, L. 2014 Analysis of fluid systems: stability, receptivity, sensitivity. *Appl. Mech. Rev.* **66** (2), 024803.

SCHMID, P. J. & HENNINGSON, D. S. 2001 *Stability and Transition in Shear Flows*. Springer.

SCHNEIDER, J. M. & WATSON, P. K. 1970 Electrohydrodynamic stability of space-charge-limited currents in dielectric liquids. I. Theoretical study. *Phys. Fluids* **13** (8), 1948–1954.

SCHOPPA, W. & HUSSAIN, F. 1998 A large-scale control strategy for drag reduction in turbulent boundary layers. *Phys. Fluids* **10** (5), 1049–1051.

SOLDATI, A. & BANERJEE, S. 1998 Turbulence modification by large-scale organized electrohydrodynamic flows. *Phys. Fluids* **10** (7), 1742–1756.

TRAORÉ, P. H. & PÉREZ, A. T. 2012 Two-dimensional numerical analysis of electroconvection in a dielectric liquid subjected to strong unipolar injection. *Phys. Fluids* **24** (3), 037102.

TREFETHEN, L. N., TREFETHEN, A. E., REDDY, S. C. & DRISCOLL, T. A. 1993 Hydrodynamic stability without eigenvalues. *Science* **261** (5121), 578–584.

WEIDEMAN, J. A. & REDDY, S. C. 2000 A MATLAB differentiation matrix suite. *ACM Trans. Math. Softw.* **26** (4), 465–519.

WU, J., TRAORÉ, P., VÁZQUEZ, P. A. & PÉREZ, A. T. 2013 Onset of convection in a finite two-dimensional container due to unipolar injection of ions. *Phys. Rev.* E **88**, 053018.

ZHANG, M., LASHGARI, I., ZAKI, T. A. & BRANDT, L. 2013 Linear stability analysis of channel flow of viscoelastic Oldroyd-B and FENE-P fluids. *J. Fluid Mech.* **737**, 249–279.

https://doi.org/10.1017/jfm.2015.134 Published online by Cambridge University Press